

Solid-State Lifshitz-van der Waals Repulsion through Two-Dimensional Materials

Tian Tian ^{*1}, Gianluca Vagli ^{*1}, Franzisca Naef¹, Kemal Celebi¹, Yen-Ting Li^{2, 3},
Shu-Wei Chang², Frank Krumeich⁴, Elton J. G. Santos^{5,6}, Yu-Cheng Chiu², and
Chih-Jen Shih ^{†1}

¹Institute for Chemical and Bioengineering, ETH Zürich, CH-8093 Zürich,
Switzerland

²Department of Chemical Engineering, National Taiwan University of Science
and Technology, Taipei 10607, Taiwan

³National Synchrotron Radiation Research Center, Hsinchu 30076, Taiwan

⁴Laboratory of Inorganic Chemistry, ETH Zürich, 8093, Zürich, Switzerland

⁵Institute for Condensed Matter Physics and Complex Systems, School of Physics
and Astronomy, The University of Edinburgh, EH9 3FD, UK.

⁶Higgs Centre for Theoretical Physics, The University of Edinburgh, EH9 3FD,
United Kingdom

^{*}These authors contributed equally to this work.

[†]Corresponding author. Email: chih-jen.shih@chem.ethz.ch

In the 1960s, Lifshitz et al. predicted that quantum fluctuations can change the van der Waals (vdW) interactions from attraction to repulsion. However, the vdW repulsion, or its long-range counterpart - the Casimir repulsion, has only been demonstrated in liquid. Here we show that the atomic thickness and birefringent nature of two-dimensional materials make them a versatile medium to tailor the Lifshitz-vdW interactions. Based on our theoretical prediction, we present direct force measurement of vdW repulsion on 2D material surfaces without liquid immersion and demonstrate their substantial influence on epitaxial properties. For example, heteroepitaxy of gold on a sheet of freestanding graphene leads to the growth of ultrathin platelets, owing to the vdW repulsion-induced ultrafast diffusion of gold clusters. The creation of repulsive force in nanoscale proximity offers technological opportunities such as single-molecule actuation and atomic assembly.

When two electroneutral objects, A and B, are brought in proximity in a polarizable medium, m, the correlations in their temporal electromagnetic (EM) fluctuations usually lead to an attractive interaction¹. At small separations (< 10 nm), this is the vdW force², and at large separations (> 20 nm) known as the Casimir force^{3,4}. Early vdW theories⁵⁻⁷ assumed the total interaction between two objects, each consisting of many molecules, is simply the sum of intermolecular potentials, which ignored the fact that the molecular interactions can strongly depend on surroundings. By applying quantum field theory in statistical physics, seminal work by Lifshitz et al.⁸ completely abandoned the assumption and predicted that quantum fluctuations can lead to repulsive interactions in both vdW and Casimir regimes. Their existence was later experimentally verified in a number of fluid-based systems.⁹⁻¹¹

As the interaction potential in the Lifshitz theory^{2,8} is proportional to the product of effective polarizabilities of A and B screened by m, the most straightforward approach to generate Casimir or vdW repulsion is to design a set of materials such that^{9,12}

$$(\epsilon_A - \epsilon_m)(\epsilon_B - \epsilon_m) < 0 \quad (1)$$

where ϵ_A , ϵ_B , ϵ_m are the frequency-dependent dielectric responses for A, B, and m, respectively. Accordingly, the experiments demonstrating long-range Casimir repulsion were majorly carried out in high-refractive-index fluids, i.e., m=fluid, in which ϵ_m is between ϵ_A and ϵ_B over a wide range of frequencies to obey inequality (1).

However, the examination of vdW repulsion in fluid immersion^{9,13–15} has two fundamental limitations. First, the high-refractive-index fluid medium is made by highly polar molecules, and their orientation and polarity within a small separating gap may disturb the force¹⁶. Second, more critically, the fluid dielectric response usually drops rapidly beyond the visible frequency region, lowering ϵ_m below ϵ_A and ϵ_B which results in high-frequency attraction. The long-range repulsive force observed in fluid arises from the retardation of the high-frequency contributions¹⁷, but when working at small separations, the full-spectrum summation may convert the force from repulsion to attraction¹⁷. In this respect, the demonstration of vdW repulsion in solid-state systems is clearly of fundamental and practical interests.

In principle, there is no reason why vdW repulsion cannot exist in solid-state systems. In addition to proper selection of materials fulfilling inequality (1), the major challenge is to fabricate an ultrathin medium film (m) sandwiched between two bulk materials (A and B), such that the vdW repulsion is sufficiently strong to be observed. Here we show that 2D materials-mediated systems could nicely address the challenge.

The idea of investigating the 2D materials-mediated repulsive vdW forces was inspired by recent findings of the wetting transparency^{18–22} and the remote epitaxy^{23,24} on graphene-coated substrates. In these systems, the vdW interactions exerted by the substrate (A) can be transmitted through the monolayer-containing medium (m) and greatly influence the thermodynamic properties on the other side (B), meaning that 2D materials are highly transparent to vdW interactions. We therefore predict, if the dielectric response of the 2D material medium is between ϵ_A and ϵ_B , a strong vdW repulsion may be generated.

Consider two semi-infinite bulk materials A and B separated by a gap containing a sheet of monolayer 2D material (Fig. 1a). When the separation d is larger than the vdW thickness of monolayer, we treat the separating gap containing the monolayer surrounded by vacuum as an effective birefringent medium with distinct in-plane (IP) and out-of-plane (OP) dielectric responses ϵ_m^{\parallel} and ϵ_m^{\perp} , which are functions of d and imaginary frequency $i\xi$, respectively, resulted from the different IP and OP electronic properties of the monolayer. Using the polarizability theory of 2D materials²⁵, ϵ_m^{\parallel} and ϵ_m^{\perp} are given by $\epsilon_m^{\parallel}(d) = 1 + \frac{\alpha_{2D}^{\parallel}}{\epsilon_0 d}$ and $\epsilon_m^{\perp}(d) = \left(1 - \frac{\alpha_{2D}^{\perp}}{\epsilon_0 d}\right)^{-1}$, where α_{2D}^{\parallel} and α_{2D}^{\perp} are the d -independent IP and OP polarizabilities for the 2D material extracted from first principle calculations, respectively (for details see *Methods*).

The vdW interaction potential between A and B across a birefringent medium m, Φ_{AmB}^{vdW} , is given by² (for

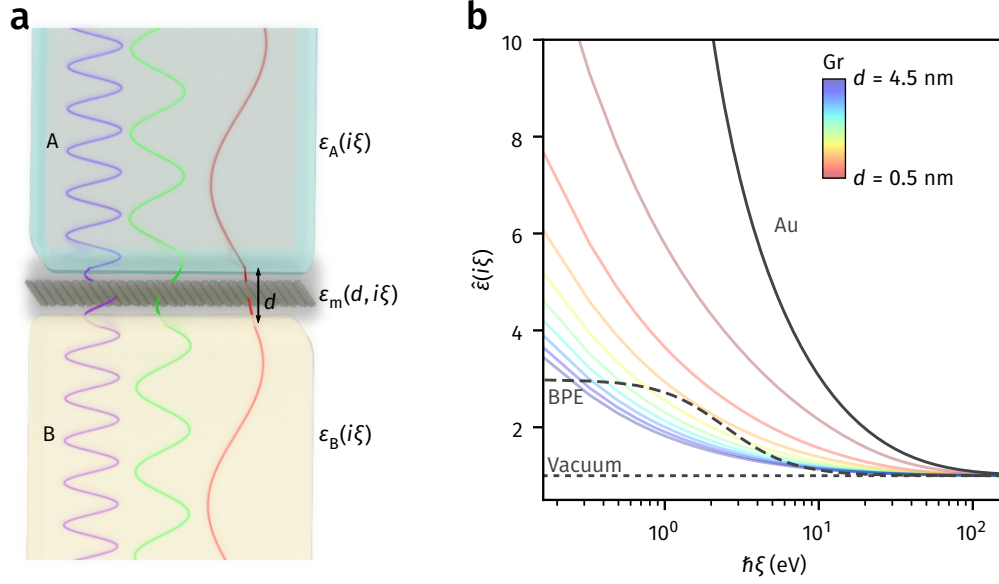


Fig. 1. **vdW repulsion in 2D materials-mediated systems.** **a.** The interaction potential between material A and B across a birefringent medium gap m containing a sheet of monolayer 2D material becomes repulsive when $[\epsilon_A(i\xi) - \hat{\epsilon}_m(d, i\xi)][\epsilon_B(i\xi) - \hat{\epsilon}_m(d, i\xi)] < 0$ at given imaginary frequency $i\xi$ and separation d . **b.** Dielectric responses for Au, BPE, Vac, and Gr at different separations as a function of electromagnetic energy, $\hbar\xi$, for different separations. Accordingly, we predict that vdW repulsion may be observed in two sets of materials, $A/m/B = \text{Vac}/\text{Gr}/\text{Au}$ and $\text{Au}/\text{Gr}/\text{BPE}$.

details see *Methods*):

$$\Phi_{\text{AmB}}^{\text{vdW}}(d) = \sum_{n=-\infty}^{\infty} G_{\text{AmB}}(i\xi_n) = \sum_{n=-\infty}^{\infty} \frac{k_B T g_m(i\xi_n)}{16\pi d^2} \left\{ \int_n^{\infty} q \ln [1 - \Delta_{\text{Am}}(i\xi_n) \Delta_{\text{Bm}}(i\xi_n) e^{-q}] d \right\} \quad (2)$$

where k_B is the Boltzmann constant, T is the absolute temperature, $\xi_n = 2\pi n k_B T / \hbar$ is the n -th Matsubara frequency, \hbar is the reduced Planck constant, $r_n = \frac{2d\xi_n}{c} \sqrt{\hat{\epsilon}_m}$ is the retardation factor², c is the speed of light in vacuum and q is a dimensionless auxiliary variable. $\hat{\epsilon}_m = \sqrt{\epsilon_m^{\parallel} \epsilon_m^{\perp}}$ and $g_m = \epsilon_m^{\perp} / \epsilon_m^{\parallel}$ are the geometrically-averaged dielectric function and dielectric anisotropy²⁵ of m , respectively. Similar approach was also used to calculate vdW interactions of layered materials²⁶. Δ_{Am} and Δ_{Bm} correspond to the dielectric mismatches following $\Delta_{\text{jm}} = \frac{\hat{\epsilon}_j - \hat{\epsilon}_m}{\hat{\epsilon}_j + \hat{\epsilon}_m}$, for $j = A, B$. Analogous to inequality (1), the vdW potential for a given EM mode ξ_n becomes positive when $\Delta_{\text{Am}} \Delta_{\text{Bm}} < 0$, contributing to vdW repulsion.

Using graphene (Gr), the thinnest carbon-based 2D material, as a model system, the calculated $\hat{\epsilon}_m$ as a function of $\hbar\xi$ for different separations are shown in Fig. 1b. The dielectric responses have the same order of magnitude with those for high-refractive-index fluids^{9,10,17} (Supplementary Fig. S1) but the applicable

separation appears to be significantly smaller. Indeed, equation (2) suggests that the vdW repulsion can be tuned by the separation d and the dielectric anisotropy g_m , which highlight the versatility of 2D materials-mediated systems. Fig. 1b also includes the dielectric responses for the three bulk materials considered in our experiments later, including gold (Au), N,N'-bis(2-phenylethyl)perylene-3,4,9,10-bis(dicarboximide) (BPE)^{27,28} molecular solid, and vacuum (Vac). It reveals that vdW repulsion may be observed in two sets of materials, A/m/B = Vac/Gr/Au and Au/Gr/BPE, in which the former obeys inequality (1) in all separations and frequencies and the latter for separations < 2 nm.

As pointed out in several theoretical studies^{22,26}, for an A/m/B system where m is a layer of 2D material, the total vdW potential consists of both attractive and repulsive contributions. Taking the Vac/Gr/Au system as an example, the gold layer on freestanding graphene is expected to not only experience a repulsive potential, $\Phi_{\text{Rep}} = \Phi_{\text{AmB}}^{\text{vdW}}$, but also an attractive potential, Φ_{Att} , corresponding to the two-body vdW potential between gold and graphene, $\Phi_{\text{mB}}^{\text{vdW}}$. The total potential acting on gold, $\Phi_{\text{tot}} = \Phi_{\text{Att}} + \Phi_{\text{Rep}}$, combines both effects. Our calculations based on equation (2) show that Φ_{Rep} is of relatively longer-range, scaling as $d^{-1.5}$ to $d^{-2.5}$, for separations from ~ 1 nm to ~ 10 nm, as compared to Φ_{Att} scaling as $d^{-2.4}$ to $d^{-2.9}$ (Fig. 2a). As a result, for $d > 3$ nm, the first derivative of $-\Phi_{\text{tot}}$ is positive, thereby yielding a net repulsive force between gold and vacuum through monolayer graphene.

According to our theoretical prediction, we carried out direct measurement for the vdW force experienced by a gold-coated tip in atomic force microscopy (AFM) interacting with a sheet of freestanding graphene (Fig. 2b). The freestanding graphene was fabricated by transferring a piece of micro-mechanically-exfoliated graphene to a holey silicon nitride (SiN_x) membrane supported by a silicon chip²⁹, with the hole diameter of approximately $5 \mu\text{m}$, followed by annealing it in Ar/H_2 to remove contaminants^{30,31}. A gold-coated AFM tip with a measured radius of 33 nm was chosen for the force-distance measurements (for details see Supplementary Section S1). All measurements were carried out in air. Supplementary Figs S5a and S5b show representative force-distance responses for the approach/retraction processes on freestanding and SiN_x -supported graphene, respectively (measurement details see Supplementary Section S3). Note that when establishing the contact, the force response is quadratic for freestanding graphene, in contrast to the linear response on supported region. This is expected considering the mechanical flexibility of freestanding graphene membrane, which yields elastic response of higher order³². Indeed, during the retraction process from a freestanding graphene surface, the tip remains to adhere to graphene at a large tip displacement, revealing that both graphene and AFM cantilever were bent before overcoming the attractive two-body interaction Φ_{Att} .

With the nonideality in mind, hereafter, we focus on the approach responses before physical contact with the sample surface.

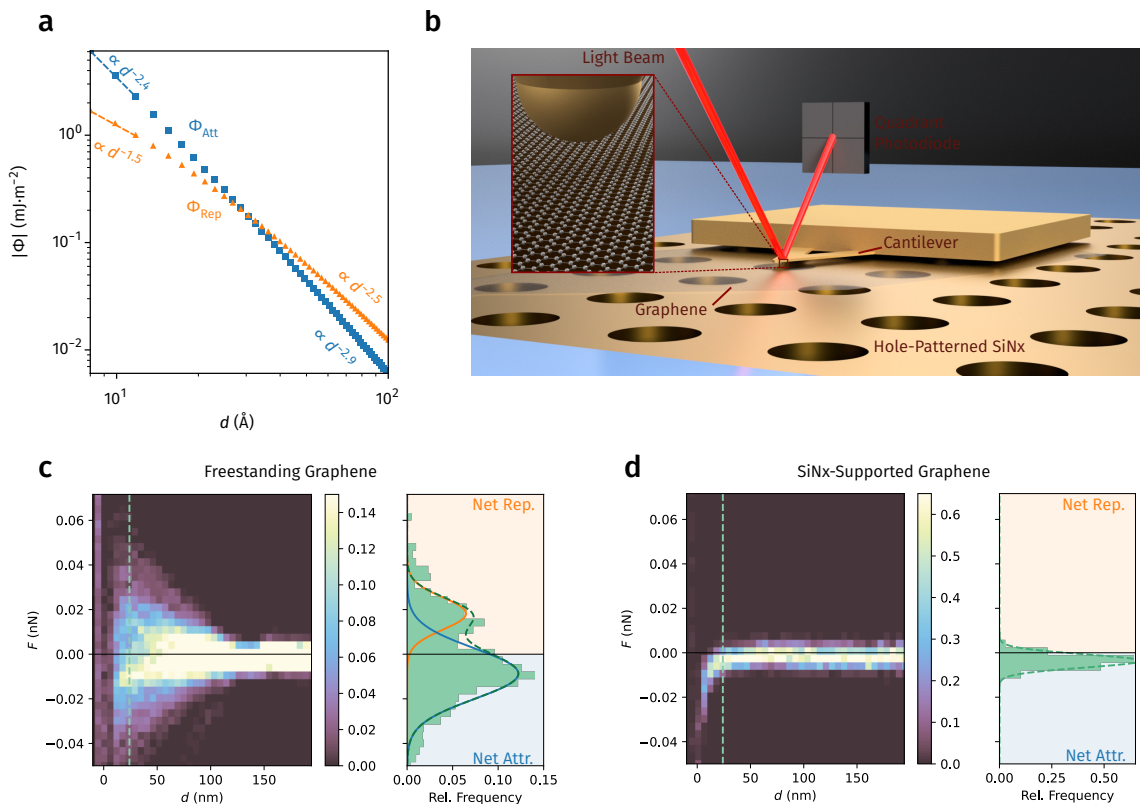


Fig. 2. Direct measurement of vdW repulsion on freestanding graphene. **a.** Calculated many-body repulsive potential, $\Phi_{\text{Rep}} = \Phi_{\text{AmB}}^{\text{vdW}}$, and two-body attractive potential, $\Phi_{\text{Att}} = \Phi_{\text{mB}}^{\text{vdW}}$, as a function of d . The former is of relatively long-range, scaling as $d^{-1.5}$ to $d^{-2.5}$, as compared to the latter scaling as $d^{-2.4}$ to $d^{-2.9}$, thereby yielding an energy barrier above graphene surface. **b.** Experimental setup for measuring the force responses between a gold-coated spherical AFM tip and a piece of micro-mechanically-exfoliated graphene transferred onto a holey SiN_x windows. **c, d.** 2D-histograms sampling **c.** 225 measurements over a $3.44 \mu\text{m} \times 3.44 \mu\text{m}$ large area on freestanding graphene and **d.** 36 measurements over a $1.37 \mu\text{m} \times 1.37 \mu\text{m}$ large area of SiN_x -supported graphene. The right panels show the force distribution at $d \approx 24$ nm corresponding to the green dashed lines on the histograms. More than 90 measurements showed repulsive behavior. The distribution on freestanding graphene is bimodal, clearly showing a population of repulsive forces.

Figs 2c and 2d compare the two-dimensional histograms for the force-distance responses extracted from 225 and 36 measurements on freestanding and SiN_x -supported graphene, respectively. The right panels present the force distributions at $d \approx 24$ nm corresponding to the green dashed lines on the two-dimensional histograms. Remarkably, more than 90 measurements showed repulsive behavior (representative response in Supplementary Fig. S6). The force distribution on freestanding graphene (2c) is bimodal, which can be

nically decomposed to two Gaussian functions, revealing one population located at the repulsive regime (mean force $\mu = 18.2$ pN and standard deviation $\sigma = 7.2$ pN). The attractive population ($\mu = -8.7$ pN and $\sigma = 11.3$ pN) presumably comes from the responses characterized on the area contaminated by airborne adsorbates³⁰, as well as the impurities introduced in process history, including transfer and scanning electron microscopy³³. On the other hand, measurements on supported graphene (Fig. 2d) only yield attractive responses ($\mu = -3.7$ pN and $\sigma = 3.0$ pN). The theoretical picture presented in Fig. 2a suggests that the directly measured repulsive force corresponds to the force required to overcome the repulsive energy barrier before the short-range attractive interaction overtakes. Given the tip radius characterized in SEM (33 nm), we calculated the height of repulsive energy barrier by integrating the average force response in the repulsive population with respect to d , yielding a value of $19 \pm 5 \mu\text{J}\cdot\text{m}^{-2}$ (see Supplementary Section S3.3), which nicely agrees with our theoretical prediction ($20 \mu\text{J}\cdot\text{m}^{-2}$; see Supplementary Fig. S2).

We have found that the vdW repulsion generated in Vac/Gr/Au system is sufficiently strong to alter the epitaxial properties of Au grown on freestanding graphene. As schematically shown in Fig. 3a, we evaporated a small amount ($\sim 3 \text{ ng}\cdot\text{mm}^{-2}$) of gold that condensed on a sheet of freestanding graphene in high vacuum at room temperature (for details see *Methods*). Fig. 3b shows a representative scanning electron micrograph (SEM) for gold deposited on graphene. Two regions, namely amorphous carbon (a-C) grid-supported (I) and freestanding (II) graphene, can be identified in the inset SEM image. The morphology and density for the deposited gold clusters on regions I and II exhibit substantially different features. On region I, as expected, due to a very high surface energy of gold ($\sim 1300 \text{ mJ}\cdot\text{m}^{-2}$ at room temperature³⁴), fast condensation at room temperature yields small spherical nanoclusters with a high nucleation density. However, on region II, despite a high degree of supercooling, the nucleation density is very low, leaving a large non-wettable area of up to $1.3 \mu\text{m}^2$, with a few large and ultrathin gold platelets grown on the surface. We performed crystallographic analysis using the Fourier-transformed scanning transmission electron microscopy (FT-STEM) on a representative hexagonal platelet (Fig. 3c). A set of Bragg diffraction spots corresponding to $\{\frac{4}{3} \frac{2}{3} \frac{2}{3}\}$ lattice planes (lattice spacing of $\sim 2.49 \text{ \AA}$) was observed, which was only reported in the atomically-thin face-center-cubic metal crystals³⁵. We also notice that gold deposited on the defective and contaminated domains of freestanding graphene, e.g., region III, exhibits similar behavior with that on region I.

From a thermodynamic point of view, the growth of ultrathin gold platelets on freestanding graphene would require the Au-Gr interactions to be stronger than Au surface energy, or even a negative interfacial tension³⁶, which is unlikely and cannot explain the observed ultralow nucleation density. We further trans-

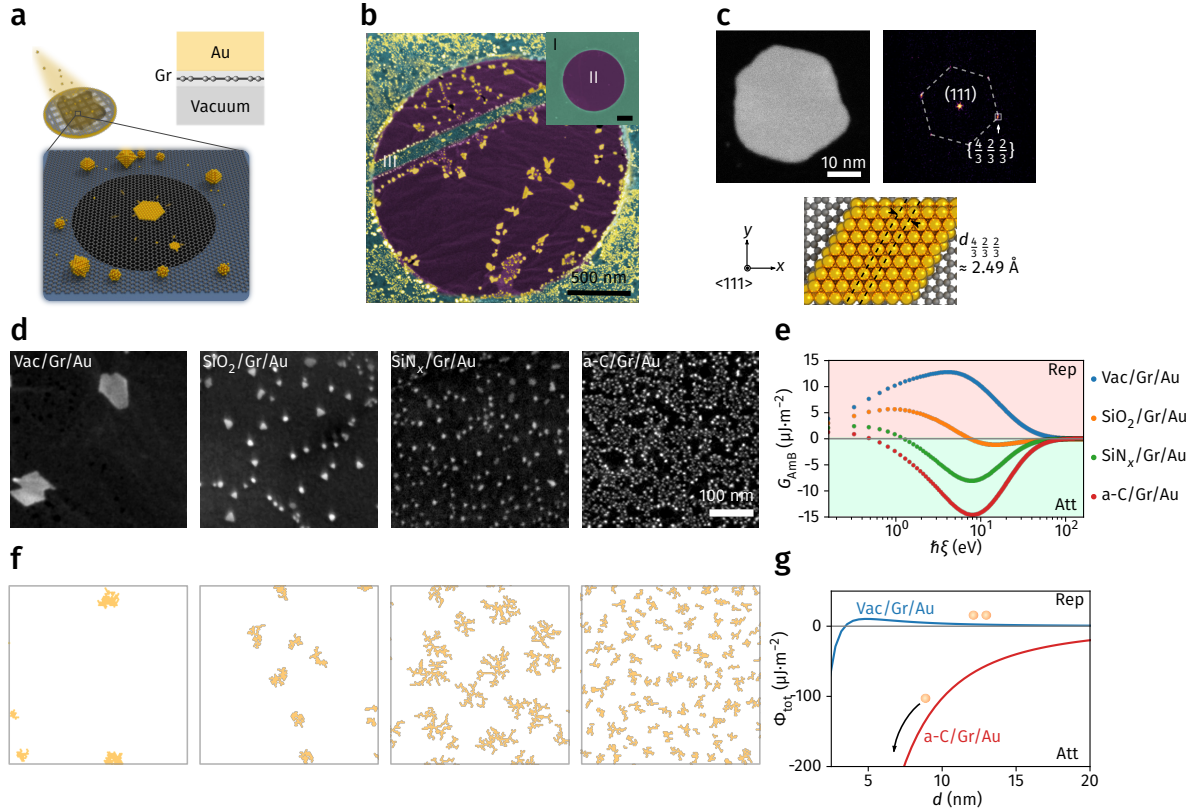


Fig. 3. Ultrafast diffusion of gold atoms on freestanding graphene at room temperature. **a.** A small amount of gold was evaporated in high vacuum and condensed at room temperature on a sheet of freestanding graphene transferred to a Quantifoil holey carbon grid. **b.** False color SEM image for gold deposited on graphene near a hole. Inset: SEM image before gold deposition that identifies regions I and II corresponding to carbon grid-supported and freestanding graphene, respectively. Gold on freestanding graphene forms ultrathin platelets and leaves a large non-wettable area of up to $1.3 \mu\text{m}^2$. **c.** FT-STEM characterization of a representative hexagonal platelet (left), revealing a set of Bragg diffraction spots (right) corresponding to $(4/3 \ 2/3 \ 2/3)$ lattice plane (d -spacing of $\sim 2.49 \text{ \AA}$). **d.** SEM images for gold deposited on graphene supported by different substrates (left to right: vacuum, SiO_2 , SiN_x , and amorphous carbon (a-C)). **e.** Calculated interaction spectra G_{AmB} as a function of $\hbar\xi$ at $d = 0.8 \text{ nm}$ for Vac/Gr/Au, $\text{SiO}_2/\text{Gr}/\text{Au}$, $\text{SiN}_x/\text{Gr}/\text{Au}$ and a-C/Gr/Au, respectively. The full-spectrum summation is gradually converted from repulsion to attraction, yielding the increase of nucleation density in **D**. **f.** KMC simulation snapshots modeling 2D growth of gold on a surface by varying the ratio of activation energy for diffusion on pristine graphene, ΔE_d^0 , to that for binding, ΔE_b (left to right: $\Delta E_d^0/\Delta E_b = 0.2, 0.5, 1.0, 1.6$). **g.** Calculated Φ_{tot} profiles for 6 nm thick gold platelet approaching freestanding (blue) and substrate-supported (red) graphene with respect to separation.

ferred graphene onto two other substrates, silicon oxide (SiO_2) and silicon nitride (SiN_x), and compared the morphologies of gold condensed on top (Fig. 3d). Fig. 3e presents the calculated many-body vdW interaction spectra as a function of energy, $G_{\text{AmB}}(i\xi)$ (see equation (2)), for the four systems considered here. The full-spectrum summation indicates that in contrast to the repulsive Vac/Gr/Au system, for $\text{SiO}_2/\text{Gr}/\text{Au}$, $\text{SiN}_x/\text{Gr}/\text{Au}$, and a-C/Gr/Au, the vdW interactions become increasingly attractive. Together with Fig. 3d, it becomes evident that stronger vdW repulsion would lead to lower nucleation density. The growth behavior is kinetically controlled which agrees with morphological statistics of the gold nanoplatelets based on AFM and SEM analysis (for details see Supplementary Section S4.3). We further exclude the scenario of remote epitaxy²³ or “lattice transparency”³⁷ of graphene, since the highest crystalline samples were obtained on free-standing graphene, contradicting the polarity-dominated mechanism of remote epitaxy²⁴ (more discussions see Supplementary Section S6.1).

density N_{nu} is proportional to $D^{-\frac{1}{3}}$, where D is the surface diffusivity³⁸. Indeed, the classical nucleation theory suggests that the nucleation D is the surface diffusivity³⁸. According to the SEM images in Fig. 3d, we estimate that, by making graphene freestanding, the surface diffusivity of gold was boosted by up to approximately 9 orders of magnitude (Supplementary Fig. S19, right y-axis), indicating ultrafast in-plane diffusion. The platelets grown on freestanding graphene can be over 10^2 times larger than that on a-C/Gr, indicating that the platelet growth is dominated by kinetic effect rather than thermodynamic wettability. The observation is further endorsed by our kinetic Monte Carlo (KMC) simulations considering the competition between Au diffusion on graphene and Au-Au binding processes on a surface (Fig. 3f and Supplementary Fig. S21). Large and sparsely distributed platelets can only be obtained when the activation energy for diffusion is negligible compared to that for Au-Au binding (see Supplementary Section S4.4).

The repulsive potential predicted by the Lifshitz model not only makes the surface adsorption an energy uphill process at large separation, but also decreases the vdW potential well depth at the contact distance by nearly 50% (Supplementary Fig. S2), which further decrease the adsorption rate of gold onto freestanding graphene as predicted by classical aggregation theory³⁹. As such, the vdW repulsion-induced energy barrier created above the surface offers a “highway” for in-plane diffusion (Fig. 3g), forming large platelets.

The second set of materials examined here is Au/Gr/BPE (Fig. 4a). The BPE molecule has a flat polycyclic aromatic core, perylenetetracarboxylic diimide (PTCDI), decorated with two freely rotatable phenylethyl groups on both ends. Highly ordered BPE molecular solids are of layered crystalline structure²⁸, with the interlayer spacing determined by the sensitive balance between intermolecular $\pi - \pi$ interactions of PTCDI

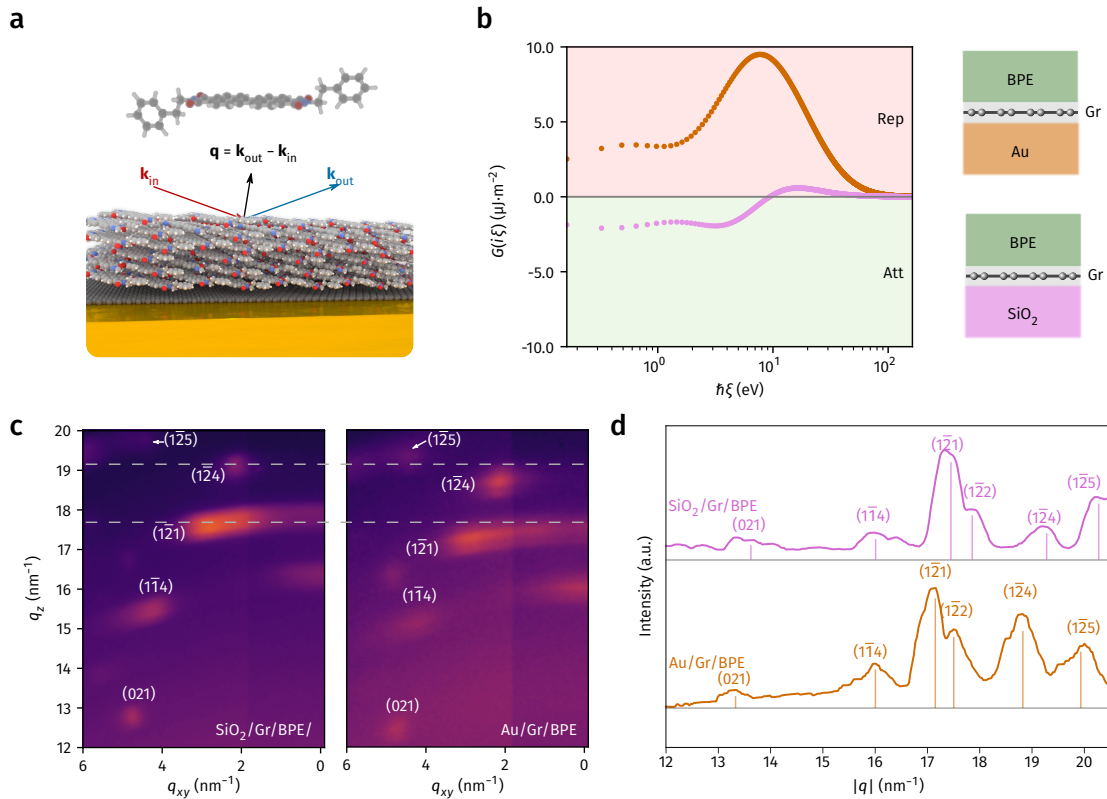


Fig. 4. vdW repulsion-induced molecular polymorphism. **a.** Molecular structure of BPE (top) and schematic of molecular solid (bottom) having a layered crystalline structure, with the molecular plane oriented in parallel to graphene. The diffraction wave vector \mathbf{q} of a specific lattice plane follows the relation $\mathbf{q} = \mathbf{k}_{\text{out}} - \mathbf{k}_{\text{in}}$, where \mathbf{k}_{in} and \mathbf{k}_{out} are the wave vectors of incident and diffracted light in GIWAXS, respectively. **b.** Calculated interaction spectra $G_{\text{AmB}}(i\xi)$ as a function of $\hbar\xi$ for Au/Gr/BPE (orange dots) and SiO₂/Gr/BPE (purple dots) systems at $d = 1$ nm, revealing that the former yields a strong vdW repulsion and the latter has a weak attraction. **c.** Magnified GIWAXS patterns for SiO₂/Gr/BPE (left) and Au/Gr/BPE (right) systems showing the Laue spots corresponding to inter-layer planes (124) and (121) near the q_z axis. As compared to SiO₂/Gr/BPE, the q_z components for Au/Gr/BPE are slightly lower, confirming the interlayer d-spacings are enlarged. **d.** Comparison of integrated line cuts for SiO₂/Gr/BPE, Au/Gr/BPE. The best-fitted peak positions are marked as vertical lines.

cores and phenylethyl groups conformational entropy⁴⁰. We therefore hypothesized that, by orienting the BPE molecular plane parallel to graphene, the force exerted by the substrate across graphene may alter the interlayer spacing.

The BPE molecules were thermally evaporated onto graphene supported by gold as well as SiO₂ for comparison (Fig. 4b, for details see *Methods*). Fig. 4b presents the calculated $G_{\text{AmB}}(i\xi)$ for the two systems at $d = 0.8$ nm. Following earlier discussion in Fig. 1b, for $d < 2$ nm, the vdW potentials between Au and BPE are always repulsive irrespective of frequency, with the main contribution from the visible to ultraviolet region. The full-spectrum summation of $G_{\text{AmB}}(i\xi)$ according to equation (2) yields a strong vdW repulsion of ~ 1.3 mJ·m⁻². On the other hand, in SiO₂/Gr/BPE system, the transition from attraction to repulsion at high frequencies leads to a weakly attractive potential (~ -20 μJ·m⁻²).

To examine the substrate interactions through graphene, we analyzed the molecular orientation and crystallographic constants of BPE molecular solids using synchrotron grazing-incidence wide-angle x-ray scattering (GIWAXS). In the GIWAXS patterns (Fig. 4c and Supplementary Fig. S27), both systems show several intense high-angle Laue spots, in particular those corresponding to the interlayer ($\bar{1}\bar{2}4$) and ($\bar{1}\bar{2}1$) planes (detailed crystallographic analysis see Supplementary Section S5) near the q_z axis, confirming the PTCDI plane is preferentially oriented parallel to the substrate^{41,42}. However, the slightly shifted q_z components reveal polymorphs induced by the substrate force (Fig. 4c). The strongly repulsive substrate, gold, yielded interlayer spacings of 3.35 and 3.68 Å, respectively, which are enlarged by $\sim 1.8\%$ as compared to the SiO₂ control. The integrated line cuts extracted from GIWAXS patterns (Fig. 4d) compares the signals for SiO₂/Gr/BPE and Au/Gr/BPE. The vdW repulsion generated in Au/Gr/BPE appears to slightly offset the interlayer interactions between BPE molecules. Consequently, the effect of phenylethyl groups conformational entropy takes a more active role, increasing the interlayer spacing for a set of high- q diffraction peaks (($\bar{1}\bar{1}4$), ($\bar{1}\bar{2}1$), ($\bar{1}\bar{2}2$), ($\bar{1}\bar{2}4$) and ($\bar{1}\bar{2}5$)) associated with the PTCDI basal plane. Further experimental examination of molecular packing on graphene-free substrates indicates the breakdown of classical vdW transparency theory in this system (more details see Supplementary Sections S5.3 and S6.1).

We have presented direct force measurement of the vdW repulsion at 2D materials surfaces and demonstrated that the vdW repulsion can substantially influence kinetics and thermodynamics of heteroepitaxy. Our findings imply that the recently reported quantum levitation^{9,11,16} might be even realized without liquid immersion, which give rise to robust solid-state device miniaturization. In addition, in view of the growth of 2D materials family covering an increasingly large range of properties, they could become versatile surface

coatings selectively repelling objects down to atomic level, which may lead to new molecular mechanical systems and sensors.

Author Contributions

T.T., G.V. and C.J.S. conceived the idea and designed the experiments. T.T. and F.N. developed the theoretical framework. T.T. performed first-principle calculations under guidance of E.J.G.S. G.V. carried out AFM force measurement, analyzed the data, and modeled the force responses. T.T., G.V. and K.C. fabricated the freestanding graphene samples and carried out Au deposition. T.T. characterized the freestanding graphene samples. F.K. performed STEM measurements. T.T. carried out KMC simulations. T.T. transferred graphene onto gold and SiO₂ substrates. Y.T.L. and S.W.C. deposited BPE molecules and carried out synchrotron GIWAXS under supervision of Y.C.C. T.T., Y.T.L. and Y.C.C. analyzed the GIWAXS patterns. T.T., G.V. and C.J.S. co-wrote the paper. All authors contributed to this work, read the manuscript, discussed the results, and agreed to the contents of the manuscript and supplementary materials.

Acknowledgments

C.J.S. is grateful for financial support from ETH startup funding and the European Research Council Starting Grant (N849229 CQWLED). T.T. G.V. and K.C. acknowledge technical support from the Scientific Center for Optical and Electron Microscopy (ScopeM) and FIRST-Center for Micro- and Nanoscience of ETH Zurich. EJGS acknowledges computational resources through the UK Materials and Molecular Modeling Hub for access to THOMAS supercluster, which is partially funded by EPSRC (EP/P020194/1); CIRRUS Tier-2 HPC Service (ec131 Cirrus Project) at EPCC (<http://www.cirrus.ac.uk>) funded by the University of Edinburgh and EPSRC (EP/P020267/1); ARCHER UK National Supercomputing Service (<http://www.archer.ac.uk>) via d429 Project code, and the UKCP consortium (Project e89) funded by EPSRC grant ref EP/P022561/1. EJGS also acknowledges the EPSRC Early Career Fellowship (EP/T021578/1) and the University of Edinburgh for funding support. Y.C.C. thanks the financial support by the “Advanced Research Center for Green Materials Science and Technology” from The Featured Area Research Center Program within the framework of the Higher Education Sprout Project by the Ministry of Education (108L9006) and the Ministry of Science and Technology in Taiwan (MOST 108-3017-F-002-002 and 108-2221-E-011-047). T.T. thanks Dr. Liqing Zheng for providing gold substrates.

Supplementary materials

- Materials and Methods
- Supplementary Text
- Figs. S1 to S34
- Tables S1 to S4
- References (S1-S46)

References

1. Woods, L. M. *et al.* Materials perspective on Casimir and van der Waals interactions. *Rev. Mod. Phys.* **88**, 045003 (2016).
2. Parsegian, V. A. *Van der Waals Forces: A Handbook for Biologists, Chemists, Engineers, and Physicists* Cambridge Core. (2017).
3. Casimir, H. B. On the attraction between two perfectly conducting plates. *K. Ned. Akad. Wet.* **51**, 793–795 (1948).
4. Casimir, H. B. G. & Polder, D. The Influence of Retardation on the London-van der Waals Forces. *Phys. Rev.* **73**, 033001 (1948).
5. Keesom, W. The second virial coefficient for rigid spherical molecules, whose mutual attraction is equivalent to that of a quadruplet placed at their centre. *Proc. R. Acad. Sci* **18**, 636–646 (1915).
6. Maitland, G. C. *Intermolecular forces: their origin and determination* (Oxford University Press, 1981).
7. London, F. The general theory of molecular forces. *Trans. Faraday Soc.* **33**, 8b–26 (1937).
8. Dzyaloshinskii, I. E., Lifshitz, E. M. & Pitaevskii, L. P. General Theory of van der Waals' Forces. *Phys.-Uspekhi* **4**, 153–176 (1961).
9. Munday, J. N., Capasso, F. & Parsegian, V. A. Measured long-range repulsive Casimir–Lifshitz forces. *Nature* **457**, 170–173 (2009).
10. Feiler, A. A., Bergström, L. & Rutland, M. W. Superlubricity Using Repulsive van der Waals Forces. *Langmuir* **24**, 2274–2276 (2008).
11. Zhao, R. *et al.* Stable Casimir equilibria and quantum trapping. *Science* **364**, 984–987 (2019).
12. Gong, T., Corrado, M. R., Mahbub, A. R., Shelden, C. & Munday, J. N. Recent progress in engineering the Casimir effect – applications to nanophotonics, nanomechanics, and chemistry. *Nanophotonics* **10**, 523–536 (2021).
13. Milling, A., Mulvaney, P. & Larson, I. Direct Measurement of Repulsive van der Waals Interactions Using an Atomic Force Microscope. *J. Colloid Interface Sci.* **180**, 460–465 (1996).
14. Meurk, A., Luckham, P. F. & Bergström, L. Direct Measurement of Repulsive and Attractive van der Waals Forces between Inorganic Materials. *Langmuir* **13**, 3896–3899 (1997).

15. Lee, S.-w. & Sigmund, W. M. AFM study of repulsive van der Waals forces between Teflon AF™ thin film and silica or alumina. *Colloids Surf. A* **204**, 43–50 (2002).
16. Munnday, J. N. & Capasso, F. Repulsive Casimir and van der Waals Forces: From Measurements to Future Technologies. *Int. J. Mod. Phys. A* **25**, 2252–2259 (2010).
17. Boström, M., Sernelius, B. E., Brevik, I. & Ninham, B. W. Retardation turns the van der Waals attraction into a Casimir repulsion as close as 3 nm. *Phys. Rev. A* **85**, 010701 (2012).
18. Rafiee, J. *et al.* Wetting transparency of graphene. *Nat. Mater.* **11**, 217–222 (2012).
19. Shih, C.-J. *et al.* Breakdown in the Wetting Transparency of Graphene. *Phys. Rev. Lett.* **109**, 176101 (2012).
20. Li, M., Reimers, J. R., Dobson, J. F. & Gould, T. Faraday cage screening reveals intrinsic aspects of the van der Waals attraction. *Proc. Nat. Acad. Sci.* **115**, E10295–E10302 (2018).
21. Liu, X., Zhang, Z. & Guo, W. van der Waals screening by graphenelike monolayers. *Phys. Rev. B* **97**, 241411 (2018).
22. Ambrosetti, A. & Silvestrelli, P. L. Hidden by graphene – Towards effective screening of interface van der Waals interactions via monolayer coating. *Carbon* **139**, 486–491 (2018).
23. Kim, Y. *et al.* Remote epitaxy through graphene enables two-dimensional material-based layer transfer. *Nature* **544**, 340–343 (2017).
24. Kong, W. *et al.* Polarity governs atomic interaction through two-dimensional materials. *Nat. Mater.* **17**, 999–1004 (2018).
25. Tian, T. *et al.* Electronic Polarizability as the Fundamental Variable in the Dielectric Properties of Two-Dimensional Materials. *Nano Lett.* **20**, 841–851 (2019).
26. Zhou, Y., Pellouchoud, L. A. & Reed, E. J. The potential for fast van der Waals computations for layered materials using a Lifshitz model. *2D Mater.* **4**, 025005 (2017).
27. Mizuguchi, J. N,N'-Bis(2-phenethyl)perylene-3,4:9,10-bis(dicarboximide). *Acta Cryst. C* **54**, 1479–1481 (1998).
28. Ling, M.-M. *et al.* Air-Stable n-Channel Organic Semiconductors Based on Perylene Diimide Derivatives without Strong Electron Withdrawing Groups. *Adv. Mater.* **19**, 1123–1127 (2007).

29. Schneider, G. F., Calado, V. E., Zandbergen, H., Vandersypen, L. M. K. & Dekker, C. Wedging Transfer of Nanostructures. *Nano Lett.* **10**, 1912–1916 (2010).
30. Li, Z. *et al.* Effect of airborne contaminants on the wettability of supported graphene and graphite. *Nat. Mater.* **12**, 925–931 (2013).
31. Russo, C. J. & Passmore, L. A. Controlling protein adsorption on graphene for cryo-EM using low-energy hydrogen plasmas. *Nat. Methods* **11**, 649–652 (2014).
32. Lee, C., Wei, X., Kysar, J. W. & Hone, J. Measurement of the Elastic Properties and Intrinsic Strength of Monolayer Graphene. *Science* **321**, 385–388 (2008).
33. Teweldebrhan, D. & Balandin, A. A. Modification of graphene properties due to electron-beam irradiation. *Appl. Phys. Lett.* **94**, 013101 (2009).
34. Mills, K. C. & Su, Y. C. Review of surface tension data for metallic elements and alloys: Part 1 – Pure metals. *Int. Mater. Rev.* **51**, 329–351 (2006).
35. Jin, R. *et al.* Photoinduced Conversion of Silver Nanospheres to Nanoprisms. *Science* **294**, 1901–1903 (2001).
36. Israelachvili, J. N. *Intermolecular and surface forces* Third edition (Elsevier, Academic Press, Amsterdam, 2011).
37. Chae, S. *et al.* Lattice Transparency of Graphene. *Nano Lett.* **17**, 1711–1718 (2017).
38. Mo, Y. W., Kleiner, J., Webb, M. B. & Lagally, M. G. Activation energy for surface diffusion of Si on Si(001): A scanning-tunneling-microscopy study. *Phys. Rev. Lett.* **66**, 1998–2001 (1991).
39. Fuchs, N. Zur theorie der koagulation. *Z. Phys. Chem.* **171**, 199–208 (1934).
40. Schmidt, R. *et al.* High-Performance Air-Stable n-Channel Organic Thin Film Transistors Based on Halogenated Perylene Bisimide Semiconductors. *J. Am. Chem. Soc.* **131**, 6215–6228 (2009).
41. Chiu, Y.-C. *et al.* Multilevel nonvolatile transistor memories using a star-shaped poly((4-diphenylamino)benzyl methacrylate) gate electret. *NPG Asia Mater.* **5**, e35 (2013).
42. Shih, C.-J. *et al.* Partially-Screened Field Effect and Selective Carrier Injection at Organic Semiconductor/Graphene Heterointerface. *Nano Lett.* **15**, 7587–7595 (2015).

Supplementary Material for: Solid-State Lifshitz-van der Waals Repulsion through Two-Dimensional Materials

Tian Tian ^{*1}, Gianluca Vagli ^{*1}, Franzisca Naef¹, Kemal Celebi¹, Yen-Ting Li^{2, 3},
Shu-Wei Chang², Frank Krumeich⁴, Elton J. G. Santos^{5,6}, Yu-Cheng Chiu², and
Chih-Jen Shih ^{†1}

¹Institute for Chemical and Bioengineering, ETH Zürich, CH-8093 Zürich,
Switzerland

²Department of Chemical Engineering, National Taiwan University of Science
and Technology, Taipei 10607, Taiwan

³National Synchrotron Radiation Research Center, Hsinchu 30076, Taiwan

⁴Laboratory of Inorganic Chemistry, ETH Zürich, 8093, Zürich, Switzerland

⁵Institute for Condensed Matter Physics and Complex Systems, School of Physics
and Astronomy, The University of Edinburgh, EH9 3FD, UK.

⁶Higgs Centre for Theoretical Physics, The University of Edinburgh, EH9 3FD,
United Kingdom

^{*}These authors contributed equally to this work.

[†]Corresponding author. Email: chih-jen.shih@chem.ethz.ch

S1 Materials and Methods

Calculation of vdW interaction spectra The dielectric responses as function of imaginary frequency $\epsilon(i\xi)$ was calculated using the Kramers Kronig relationship^{S1}:

$$\epsilon(i\xi) = 1 + \frac{2}{\pi} \int_0^{\infty} \frac{\omega \text{Im}[\epsilon(\omega)]}{\omega^2 + \xi^2} d\omega \quad (\text{S1})$$

where ω is the real frequency, and $\text{Im}[\epsilon(\omega)]$ is the imaginary part of complex dielectric function $\epsilon(\omega)$. Frequency-dependent dielectric functions of SiO_2 ^{S2}, SiN_x ^{S2}, bromobenzene (BrPh)^{S3}, amorphous carbon^{S4}, and Au^{S2} were extracted from experimental data, respectively. The dielectric function of BPE is estimated using the single Lorentz oscillator model following $\epsilon_{\text{BPE}}(i\xi) = 1 + \frac{\xi_p^2}{\xi_g^2 + K\xi + \xi^2}$ where $\hbar\xi_g = 2.30$ eV, $\hbar\xi_p = 3.16$, $\hbar K = 0.1$ eV, yielding an optical refractive index $n \approx 1.7$. Frequency-dependent 2D polarizabilities (α_{2D}^{\parallel} , α_{2D}^{\perp}) of graphene were obtained by *ab initio* package GPAW^{S5} using the projector augmented wave method^{S6}. Dielectric responses were calculated using random phase approximation on top of the Perdew-Burke-Ernzerhof exchange-correlation functional^{S7} with plane wave cutoff energy of 500 eV, k-point density of 15 \AA^{-1} and truncated Coulomb kernel to avoid spurious interaction from periodic images.

Graphene growth Monolayer graphene was synthesized by chemical vapor deposition (CVD). Copper (Cu) foil (99.999%, Alfa Aesar) was first cleaned by acetone, followed by isopropanol (IPA) and electrochemically polishing in a mixture of 2:1:1:0.2 deionized water (DI-H₂O) : orthophosphoric acid : ethanol : IPA under a bias of 5 V. The polished Cu foil was then annealed in a quartz tube furnace at 1060 °C under 5 Torr and 50 standard cubic centimetres per minute (sccm) of hydrogen (H₂) flow. The growth of graphene was followed by flowing 40 sccm of methane (CH₄) and 15 sccm of H₂ at 1000 °C under 5 Torr for 10 minutes. After cooling down, graphene on the backside of the Cu foil was etched by oxygen plasma.

Freestanding graphene on Quantifoil grids The Quantifoil® grids consisting of amorphous carbon film with pore opening of 1.2 ~ 5 μm supported by Au meshes were cleaned by acetone rinsing before use. The grids were placed onto the Cu foil with the holey carbon film facing graphene. By dropping ~ 5 μL of IPA onto the grid and heating the Cu foil at 120 °C, the grid was adhered to graphene/Cu by capillary force during evaporation of IPA. The Cu foil was etched at the liquid-air interface of 0.5 M ammonium persulfate (APS) solution. The APS residue was rinsed with DI-H₂O for several times. The grid was finally lifted from

the liquid-air interface and dried under gentle argon flow.

Exfoliated graphene on silicon nitride chip Graphene flakes exfoliated^{S8} from natural graphite and transferred to a silicon nitride (SiN_x) chip of 1 cm^2 size, patterned with an 12×12 hole-matrix, in which both hole-diameter and separation distance is approximately $5 \mu\text{m}$. The window with the hole-matrix was fabricated using electron beam lithography and etching. A wedging transfer method^{S9} was chosen to avoid damaging the hole-patterned structure. During transfer the polymer-graphene structure was aligned with a micro manipulator to the hole matrix.

Substrate-supported graphene Monolayer graphene supported by amorphous carbon film was prepared by the same method with that for freestanding graphene on Quantifoil grids. Graphene films supported by SiO_2 and SiN_x and gold were fabricated using a polymer-assisted transfer method. SiO_2 (300 nm thermal oxide on Si, Si-Mat) and SiN_x (100 nm LPCVD low-stress nitride on Si, University Wafer) wafers were cleaned by Piranha solution (7:3 H_2SO_4 : H_2O_2) before use. Ultraflat Au substrates were fabricated by the template-stripping method on silicon wafer^{S10}. Poly methylmethacrylate (PMMA, 4% solution in anisole) was spin-coated on CVD-grown graphene/Cu and baked at $120 \text{ }^\circ\text{C}$. The Cu foil was etched by 0.5 M APS solution. After exchanging APS solution with DI- H_2O , the PMMA/graphene film was transferred onto the desired substrate. The substrate was kept in ambient overnight and baked at $120 \text{ }^\circ\text{C}$ to enhance adhesion between substrate and graphene. The PMMA was removed by acetone and subsequently cleaned using IPA.

Au deposition Graphene samples (freestanding and substrate-supported) were all annealed under 1:1 mixture of Ar and H_2 at $600 \text{ }^\circ\text{C}$ for 2 hours to remove airborne contamination and loaded in high-vacuum evaporation chamber (Plassys MEB550S). Au was deposited by electron beam evaporation at room temperature under a pressure $< 10^{-7}$ mBar. The deposition rate was maintained $\sim 5 \times 10^{-3} \text{ nm}\cdot\text{s}^{-1}$. The amount of gold deposited m_{Au} (mass per area) was calculated using nominal thickness δ_{Au} as $m_{\text{Au}} = \delta_{\text{Au}}\rho_{\text{Au}}$, where $\rho_{\text{Au}} = 19.30 \text{ g}\cdot\text{cm}^{-3}$ is the density of gold.

BPE deposition Thin film epitaxy of BPE onto the desired substrates were carried out in a home-made physical vapor deposition (PVD) chamber at pressure below 10^{-5} mBar while the substrates are heated up to $80 \text{ }^\circ\text{C}$ to facilitate formation of crystalline structures. The deposition rate was kept at $0.1 \text{ nm}\cdot\text{s}^{-1}$ and final thickness of BPE was $\sim 50 \text{ nm}$.

GIWAXS characterizations GIWAXS analysis was conducted on beamline BL13A at the National Synchrotron Radiation Research Center of Taiwan. The incidence angle and beam energy of the X-ray were 0.12 and 12.16 keV, corresponding to a wavelength of 1.02143 Å. All of GIWAXS images were collected in reflection mode by MAR165 CCD with a 2D area detector.

Electron microscopy SEM characterizations were carried out on Zeiss ULTRA plus with 3 kV beam voltage and 20 μm aperture. Scanning transmission electron microscopy (STEM) images were acquired with a high-angle annular dark field (HAADF) detector both at cryogenic conditions using a liquid-nitrogen-cooled holder (Gatan) on a Hitachi HD 2700 CS (operation voltage 200 kV). Fourier transformation was performed on the phase contrast images.

AFM characterizations AFM topographies of graphene samples were performed on Bruker Resolve using the PeakForce Tapping mode combined with ScanAsyst Air ultrasharp probe to overcome noise artifacts on freestanding films caused by standard tapping mode scanning^{S11}. Force setpoint were maintained under 500 pN to avoid breaking of graphene sheet.

KMC simulations 2D diffusion of Au atoms on graphene surface was simulated by standard n-fold KMC algorithm on a triangular lattice with at least 200 mesh grids in both *x*- and *y*-directions. The following three events were considered: (i) deposition of atoms, (ii) diffusion on pristine graphene, (iii) diffusion on defective area and (iv) interatomic binding, corresponding to kinetic energy barriers of ΔE_e , ΔE_d^0 , ΔE_d^* and ΔE_b , respectively. Rate r_i of individual event i was calculated using $r_i = \nu_0 \exp(-\frac{\Delta E_i}{k_B T})$, where ν_0 is the rate prefactor, and the probability of event i , p_i , follows: $p_i = r_i n_i / \sum_i r_i n_i$, where n_i is the degeneracy of event i . More details for the parameters used in the simulations see Supplementary Information.

S2 Theoretical Simulations

S2.1 Modified Lifshitz theory for anisotropic media

The derivation of equation 2 is described as follows.. The vdW interaction energy of $\Phi_{\text{AmB}}^{\text{vdW}}$ corresponding to the total energy summed from all allowed EM modes^{S12}, is given by:

$$\Phi_{\text{AmB}}^{\text{vdW}} = \frac{k_B T}{2(2\pi)^2} \sum_{n=-\infty}^{\infty} \int_{r_n}^{\infty} \ln D(i\xi_n, \mathbf{k}) d^2\mathbf{k} \quad (\text{S2})$$

where $\mathbf{k} = (k_x, k_y)$ is the in-plane wavevector, and $D(i\xi_n, \mathbf{k})$ is the dispersion relation for a given geometry.

For generality, the dielectric tensor of material j has diagonal components ϵ_j^{xx} , ϵ_j^{yy} and ϵ_j^{zz} . By transforming

$\mathbf{k} = (\kappa \cos \vartheta, \kappa \sin \vartheta)$, and $g_j = \left[\frac{\epsilon_j^{xx}}{\epsilon_j^{zz}} \cos^2 \vartheta + \frac{\epsilon_j^{yy}}{\epsilon_j^{zz}} \sin^2 \vartheta \right]^{-1}$ where κ, ϑ are the corresponding polar coordinates of \mathbf{k} , the dispersion relation D of an anisotropic A/m/B layered system follows^{S1}:

$$D = 1 - \underbrace{\left[\frac{\hat{\epsilon}_A - \epsilon_m^{zz} g_m^{1/2}(\vartheta)}{\hat{\epsilon}_A + \epsilon_m^{zz} g_m^{1/2}(\vartheta)} \right]}_{\Delta_{\text{Am}}} \underbrace{\left[\frac{\hat{\epsilon}_B - \epsilon_m^{zz} g_m^{1/2}(\vartheta)}{\hat{\epsilon}_B + \epsilon_m^{zz} g_m^{1/2}(\vartheta)} \right]}_{\Delta_{\text{Bm}}} e^{-2g_m^{1/2}(\vartheta)\kappa d} \quad (\text{S3})$$

$$= 1 - \Delta_{\text{Am}}(\vartheta)\Delta_{\text{Bm}}(\vartheta)e^{-2g_m^{1/2}(\vartheta)\kappa d}$$

By further introducing an auxiliary variable $x = 2g_m^{1/2}(\vartheta)\kappa d$, it follows:

$$\Phi_{\text{AmB}}^{\text{vdW}} = \frac{k_B T}{32\pi^2 d^2} \sum_{n=-\infty}^{\infty} \int_0^{2\pi} g_m(i\xi_n, \vartheta) d\vartheta \int_{r_n}^{\infty} x dx \ln[1 - \Delta_{\text{Am}}(i\xi_n, \vartheta)\Delta_{\text{Bm}}(i\xi_n, \vartheta)e^{-x}] \quad (\text{S4})$$

Accordingly, equation (2) is obtained for $\epsilon_m^{xx} = \epsilon_m^{yy}$, i.e. g_m is independent of ϑ , which is valid for most 2D materials where the 2D lattice is hexagonal or square. Moreover, in equation (2), $\hat{\epsilon}_A$ and $\hat{\epsilon}_B$ reduce to ϵ_A and ϵ_B , respectively, when A and B are isotropic bulk materials. Time-reversal symmetry $\epsilon(i\xi) = \epsilon(-i\xi)$ is used when magnetic response of the material is negligible, therefore equation (2) only needs to be evaluated for $\xi_n \geq 0$. Moreover, our numerical analysis suggests the integral of $\Phi_{\text{AmB}}^{\text{vdW}}$ is dominated by $x \leq 5$, or equivalently $\kappa \leq 2.5(g_m d)^{-1}$. When d is in the order of 2 nm, and $g_m = 2.5$, the majority of interaction comes from EM modes with $\kappa < 0.05 \text{ \AA}^{-1}$. In other words, evaluating equation (2) using the material dielectric functions at the optical limit ($\mathbf{k} \rightarrow 0$) would preserve the accuracy of calculated Φ_{AmB} .

Complementary to Fig. 1b, Fig. S1 compares the dielectric responses of other materials studied here.

Notably, at the order of $d = 1$ nm, $\hat{\epsilon}_m$ of graphene is comparable to that of bromobenzene (BrPh), a high-refractive-index liquid commonly used in experiments demonstrating Casimir repulsion^{S3,S13}. In this respect, 2D material appears to be a promising candidate for realizing repulsive vdW interactions. However, unlike bulk liquid, $\hat{\epsilon}_m$ of a 2D material strongly depends on the separation d , making the repulsion more pronounced at short distances (the vdW regime).

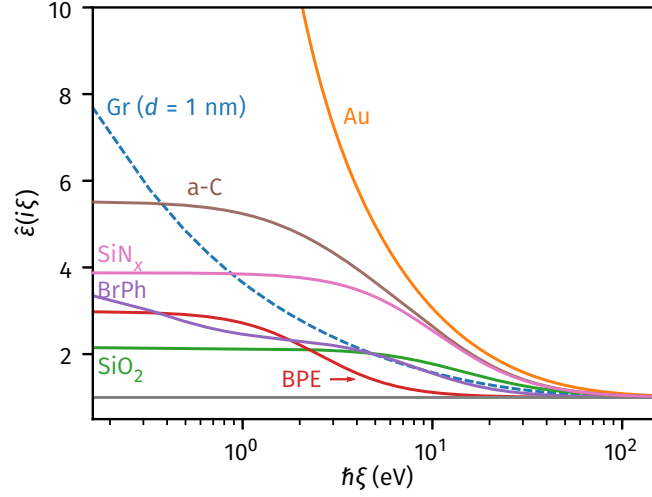


Fig. S1. **Comparison of $\hat{\epsilon}(i\xi)$ responses for materials considered in this study.** The effective dielectric function of graphene at $d = 1$ nm is higher than that of the widely-used high-refractive-index liquid bromobenzene (BrPh).

S2.2 Attractive and repulsive interactions in the Vac/Gr/Au system

The Lifshitz formalism in equation 2 corresponds to the AmB systems when A and B are semi-infinite. In order to model the interactions of atomically-thin Au platelets, a multilayer approach was used to calculate Φ_{AmB}^{vdW} as shown in Fig. S2 inset. The thickness of the Au layer is Δ_{Au} , and the effective thickness of graphene is δ_{Gr} .

The repulsive interaction Φ_{Rep} at separation d is similar to equation 2, with different expression of the

dispersion relation^{S1}:

$$\Phi_{\text{Rep}}(d, \delta_{\text{Au}}) = \frac{k_{\text{B}}T}{16\pi d^2} \sum_{n=-\infty}^{\infty} \int_{r_n}^{\infty} x \ln [1 - \Delta_{\text{L}}^*(i\xi_n)\Delta_{\text{R}}^*(i\xi_n)e^{-x}] dx \quad (\text{S5})$$

$$\Delta_{\text{L}}^* = \Delta_{\text{Vac/m}}$$

$$\Delta_{\text{R}}^* = \frac{\Delta_{\text{Vac/Au}}e^{-x\frac{\delta_{\text{Au}}}{d}} + \Delta_{\text{Au/m}}}{1 + \Delta_{\text{Vac/Au}}\Delta_{\text{Au/m}}e^{-x\frac{\delta_{\text{Au}}}{d}}}$$

where the expressions for $\Delta_{\text{Vac/m}}$ and $\Delta_{\text{Au/m}}$ are analogous to those of Δ_{Am} and Δ_{Bm} in a A/m/B system, respectively.

In the platelet system, there is also two-body attractive interaction between graphene and the Au platelet. The attractive potential between freestanding graphene and Au platelet Φ_{Att} results from the vacuum spacing between the surfaces of graphene and Au^{S14,S15}. Different from the repulsive potential, the attractive potential has a shorter distance $d^* = d - \delta_{\text{Gr}}$. The graphene layer is treated as a dielectric material with the effective dielectric tensor ϵ_{Gr} same as bulk graphite and thickness δ_{Gr} . Note despite the breakdown of continuum dielectric function for atomically thin materials, such effective treatment in Lifshitz theory can still produce quantitatively correct energy values as compared to other computationally expensive approaches, such as *ab initio* quantum chemistry simulations.^{S14}. Similar to equation (S5), Φ_{Att} of the multilayer configuration is given by:

$$\Phi_{\text{Att}}(d, \delta_{\text{Au}}) = \frac{k_{\text{B}}T}{16\pi(d^*)^2} \sum_{n=-\infty}^{\infty} \int_{r_n}^{\infty} x \ln [1 - \Delta_{\text{L}}^*(i\xi_n)\Delta_{\text{R}}^*(i\xi_n)e^{-x}] dx \quad (\text{S6})$$

$$\Delta_{\text{L}}^* = \frac{\Delta_{\text{Vac/Gr}}e^{-x\frac{\delta_{\text{Gr}}}{d^*}} + \Delta_{\text{Gr/Vac}}}{1 + \Delta_{\text{Vac/Gr}}\Delta_{\text{Gr/Vac}}e^{-x\frac{\delta_{\text{Gr}}}{d^*}}}$$

$$\Delta_{\text{R}}^* = \frac{\Delta_{\text{Vac/Au}}e^{-x\frac{\delta_{\text{Au}}}{d^*}} + \Delta_{\text{Au/Vac}}}{1 + \Delta_{\text{Vac/Au}}\Delta_{\text{Au/Vac}}e^{-x\frac{\delta_{\text{Au}}}{d^*}}}$$

Equation (S6) can be further generalized to calculate the two-body attraction in the bulk Vac/Gr/Au

system, corresponding to $\delta_{\text{Au}} \rightarrow \infty$:

$$\begin{aligned}\Phi_{\text{Att}}^{\text{Bulk}}(d) &= \frac{k_{\text{B}}T}{16\pi(d^*)^2} \sum_{n=-\infty}^{\infty} \int_{r_n}^{\infty} x \ln [1 - \Delta_{\text{L}}^*(i\xi_n)\Delta_{\text{R}}^*(i\xi_n)e^{-x}] dx \\ \Delta_{\text{L}}^* &= \frac{\Delta_{\text{Vac/Gr}}e^{-x\frac{\delta_{\text{Gr}}}{d^*}} + \Delta_{\text{Gr/Vac}}}{1 + \Delta_{\text{Vac/Gr}}\Delta_{\text{Gr/Vac}}e^{-x\frac{\delta_{\text{Gr}}}{d^*}}} \\ \Delta_{\text{R}}^* &= \Delta_{\text{Au/Vac}}\end{aligned}\tag{S7}$$

Equation S7 was used to calculate Φ_{Att} in Fig. 3b. For a bulk Vac/Gr/Au system, when the separation is much larger than δ_{Gr} , we have $d \approx d^*$. We notice that when $d \rightarrow \infty$, Φ_{Att} reduces to the interaction form between a 2D sheet and semi-infinite bulk material, scaling as $\Phi_{\text{Att}} \propto d^{-3}$, while Φ_{Rep} reduces to the interaction between two semi-infinite bulk materials in vacuum, yielding $\Phi_{\text{Rep}} \propto d^{-2}$.

The difference in scaling laws between Φ_{Att} and Φ_{Rep} results in a repulsive energy barrier beyond $d > 3$ nm, as shown in Fig. S2. As expect, we observe that the barrier decreases with thinner Au layer. The calculated magnitude of the barrier ($\sim 20 \mu\text{J}\cdot\text{m}^{-2}$ in the bulk Vac/Gr/Au system) is significantly smaller than the surface energy of graphene or gold and can be overcome by thermal energy at room temperature. For example, consider a sub-monolayer of Au atoms on 2D surface with the surface coverage λ , the thermal kinetic energy can be estimated using $E_{\text{kin}} = \lambda k_{\text{B}}T N_{\text{c}}/S_{\text{c}}$ where N_{c} and S_{c} are the number of atoms and the area of the 2D unit cell, respectively. The thermal activation energy can be overcome when $\lambda > 4 \times 10^{-4}$, which is much lower than the experimental condition. Therefore, we still expect to see nucleation on the free-standing graphene surface, while the nucleation density is greatly suppressed due to the existence of such repulsive barrier.

S2.3 Attractive interactions in substrate-supported systems

The analysis in section S2.2 can be easily extended to model the interactions between substrate (Sub) - supported graphene and a thin layer of gold. Assume the substrate has isotropic dielectric response ϵ_{Sub} , the attractive interaction between a substrate-supported graphene and Au layer, $\Phi_{\text{Att}}^{\text{ss}}$ (to be distinguished from

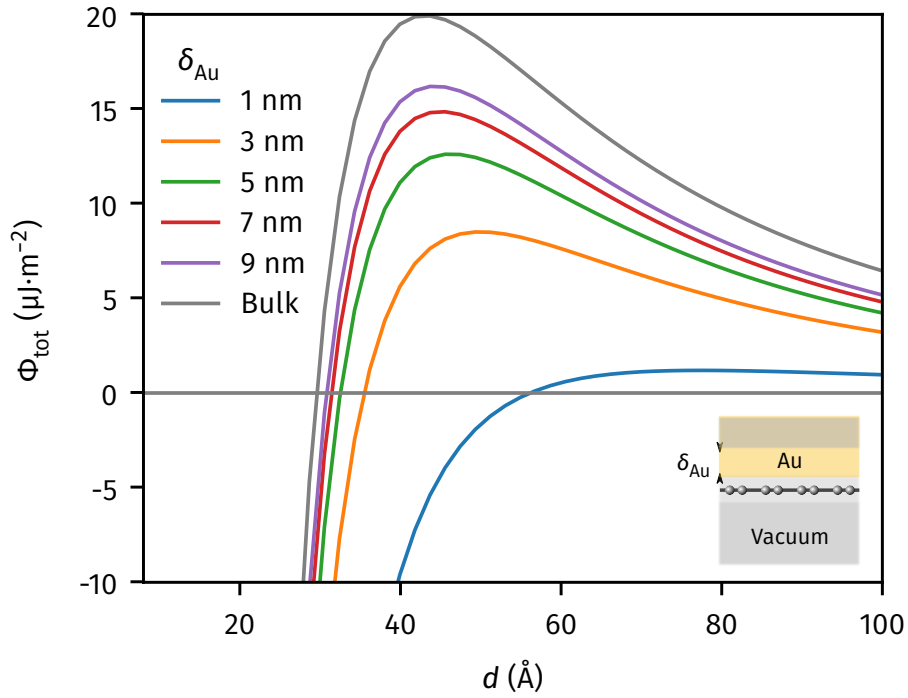


Fig. S2. **Total vdW potential Φ_{tot} as a function of Au-Gr distance d for different Au layer thickness δ_{Au} calculated from multi-layer Lifshitz approach.** A tiny repulsive potential barrier exists when $\delta_{\text{Au}} > 1$ nm, and saturates at $\sim 20 \mu\text{J}\cdot\text{m}^{-2}$ for the bulk Au layer, as a result of different power laws between attractive and repulsive interactions shown in Fig. 3b.

that of a freestanding Gr/Au system) is given by:

$$\begin{aligned}\Phi_{\text{Att}}^{\text{ss}}(d, \delta_{\text{Au}}) &= \frac{k_{\text{B}}T}{16\pi(d^*)^2} \sum_{n=-\infty}^{\infty} \int_{r_n}^{\infty} x \ln [1 - \Delta_{\text{L}}^*(i\xi_n)\Delta_{\text{R}}^*(i\xi_n)e^{-x}] dx \quad (\text{S8}) \\ \Delta_{\text{L}}^* &= \frac{\Delta_{\text{Sub/Gr}} e^{-x \frac{\delta_{\text{Gr}}}{d^*}} + \Delta_{\text{Gr/Vac}}}{1 + \Delta_{\text{Sub/Gr}} \Delta_{\text{Gr/Vac}} e^{-x \frac{\delta_{\text{Gr}}}{d^*}}} \\ \Delta_{\text{R}}^* &= \frac{\Delta_{\text{Vac/Au}} e^{-x \frac{\delta_{\text{Au}}}{d^*}} + \Delta_{\text{Au/Vac}}}{1 + \Delta_{\text{Vac/Au}} \Delta_{\text{Au/Vac}} e^{-x \frac{\delta_{\text{Au}}}{d^*}}}\end{aligned}$$

and subsequently the (two-body) attractive interaction between substrate-supported graphene and bulk gold is given by:

$$\begin{aligned}\Phi_{\text{Att}}^{\text{ss,Bulk}}(d) &= \frac{k_{\text{B}}T}{16\pi(d^*)^2} \sum_{n=-\infty}^{\infty} \int_{r_n}^{\infty} x \ln [1 - \Delta_{\text{L}}^*(i\xi_n)\Delta_{\text{R}}^*(i\xi_n)e^{-x}] dx \quad (\text{S9}) \\ \Delta_{\text{L}}^* &= \frac{\Delta_{\text{Sub/Gr}} e^{-x \frac{\delta_{\text{Gr}}}{d^*}} + \Delta_{\text{Gr/Vac}}}{1 + \Delta_{\text{Sub/Gr}} \Delta_{\text{Gr/Vac}} e^{-x \frac{\delta_{\text{Gr}}}{d^*}}} \\ \Delta_{\text{R}}^* &= \Delta_{\text{Au/Vac}}\end{aligned}$$

where the term $\Delta_{\text{Sub/Gr}}$ corresponds to the dielectric mismatch between the substrate and graphene interface. Such method is used to construct the potential-distance curve in Fig. 3H. As seen from equation (S9), $\Delta_{\text{Sub/Gr}}$ has considerable influence on the attractive potential, due to the atomic thickness of graphene (i.e. $\delta_{\text{Gr}} \ll d^*$). In other words, Φ_{Att} between Sub/Gr and gold platelet also depends on ϵ_{Sub} . Such effect is clearly different from the classical vdW description of 2D material interfaces, where the attractive two-body potential is independent of the type of substrate^{S16,S17}. As an example, the Φ_{tot} and Φ_{Att} as functions of d for Vac/Gr/Au and a-C/Gr/Au systems when $\delta_{\text{Au}} = 6$ nm (corresponding to Fig. 3H) are shown in Fig. S3. We observe the Φ_{tot} for a-C/Gr/Au system to be significantly stronger (more negative) than that for Vac/Gr/Au over the whole d -range. Therefore, it is clear that only in Vac/Gr/Au system can an overall repulsive vdW barrier be observed.

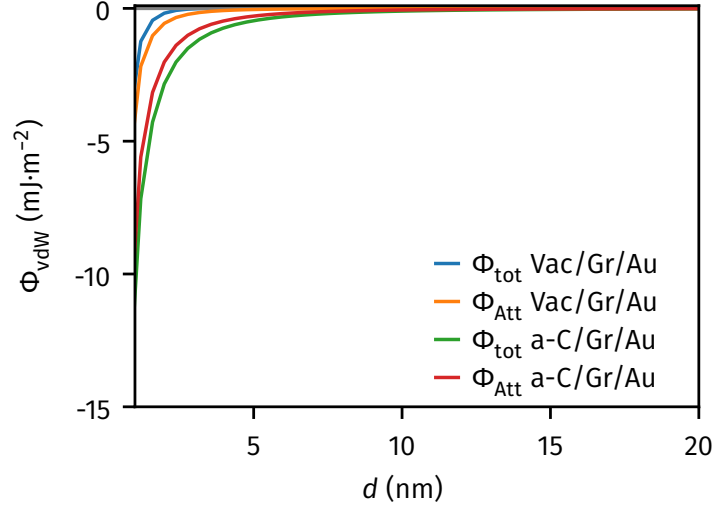


Fig. S3. Φ_{tot} and Φ_{Att} profiles as functions of d for Vac/Gr/Au and a-C/Gr/Au systems when $\delta_{\text{Au}} = 6$ nm. The $\Phi_{\text{tot}} - d$ profiles are the same as those in Fig. 3H while with much larger y -axis range. In both cases, the attractive interaction dominates at short distance.

S3 Force-distance AFM measurements

S3.1 AFM setup and calibration

The force-distance measurements were carried out with a Bruker BioScope Resolve AFM using the B side of a gold-coated NPG-10 Bruker AFM tip, with a estimated radius R_{tip} of approximately 33 nm, as highlighted with a red dashed circle in Fig. S4b. In order to obtain the interaction force (N) from the original measured values of the piezo element displacement in (mV), we carried out tip calibration steps to extract the deflection sensitivity $\left(\frac{\text{m}}{\text{V}}\right)$ and spring constant $\left(\frac{\text{N}}{\text{m}}\right)$, by using the PeakForceTMQNMTMsuite within the NanoScope[®]software environment, which determined a deflection sensitivity of $69.679 \frac{\text{nm}}{\text{V}}$ and a spring constant of $0.16136 \frac{\text{N}}{\text{m}}$. The spring constant is comparable to the nominal value of $0.12 \frac{\text{N}}{\text{m}}$ provided by the tip vendor.

S3.2 AFM background noise subtraction

The raw measurement data was processed by subtracting background noise, which was determined by fitting the force-distance measurement data with the following function:

$$f_{\text{Bkg}}(d) = p_0 + p_1 d + A \sin(\omega d + \theta) \quad (\text{S10})$$

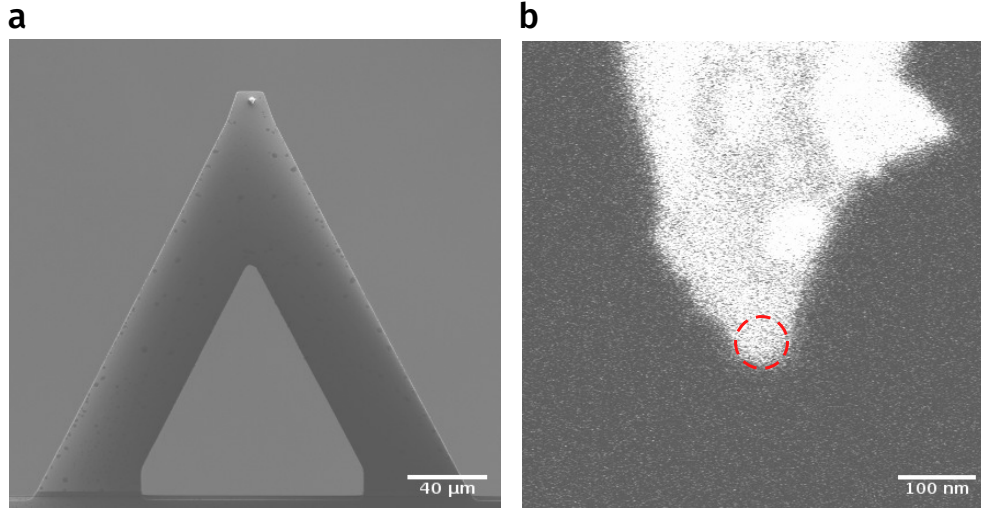


Fig. S4. **SEM images of the AFM probe considered in this study.** **a.** Top-view image of the AFM probe. The cantilever is of triangular shape with a calibrated deflection sensitivity of $69.679 \frac{\text{nm}}{\text{V}}$ and a spring constant of $0.16136 \frac{\text{N}}{\text{m}}$. **b.** Image of the AFM tip silhouette. The hemispherical shape of the tip is highlighted with a red dashed line and the radius R_{tip} was estimated to be approximately 33 nm.

within the distance range d between 150 nm to 500 nm, which is far before the tip establishes contact or after it retracts from graphene. The function f_{Bkg} contains two distinct parts of correction. The linear function $p_0 + p_1d$, could correct the noise resulting from any slant between the tip and the target. The periodic function $A \sin(\omega d + \theta)$ is to correct the optical interference noise caused by stray light reflected from the supporting material, which is a well-known phenomena taking place during force-distance measurement of reflective surfaces^{S18, S19}. This noise subtraction method is applied on both freestanding and SiN_x supported graphene, which yielded consistent results in terms of a stable baseline for further quantification, regardless of the substrate choice and whether the tip approach/retraction measurements. An example of processed force-distance hysteresis measurement is shown in Fig. S5, where Fig. S5a and S5b correspond to measurements on freestanding and SiN_x supported graphene, respectively. The distance $d = 0$ nm was set to be the point for which the force $F = 0$ N, after establishing contact. The noise-subtracted force responses exhibit well-defined zero baseline, with all essential information retained within the contact region, such as repulsive and attractive interaction, as well as the mechanical responses on freestanding and supported graphene upon retraction^{S20}.

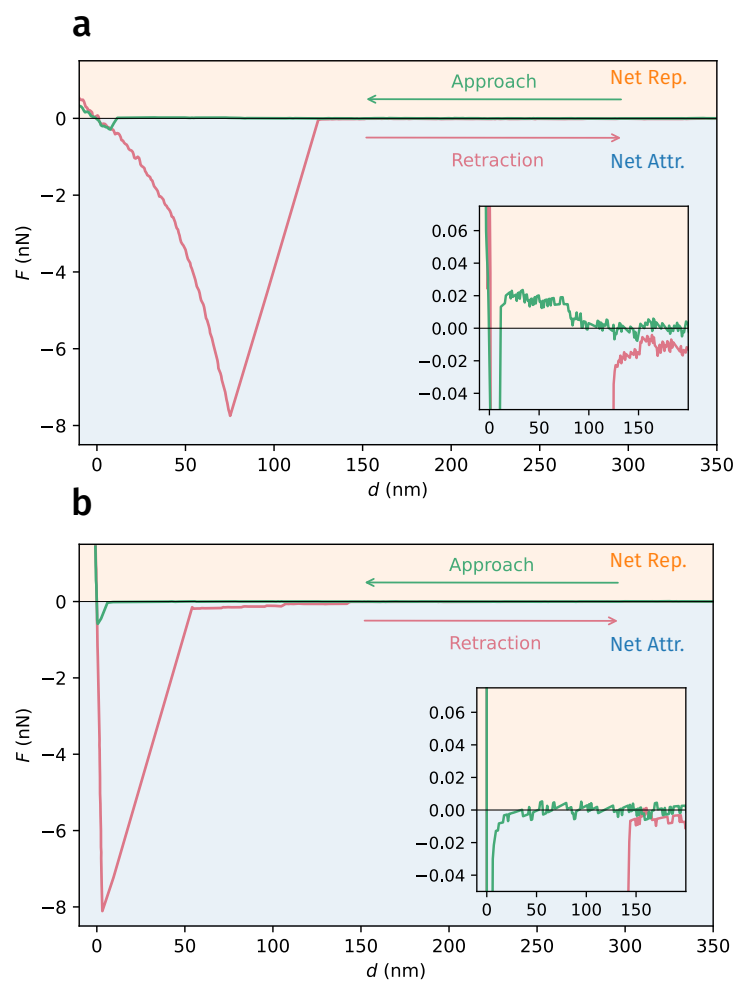


Fig. S5. **Representative force-distance responses after noise subtraction.** **a** and **b** correspond to one force-distance hysteresis measurement on freestanding and SiN_x supported graphene, respectively. The insets magnify the force responses within the contact region. Each measurement contains the approach (green) and retraction (red) responses.

S3.3 Estimation of the repulsive energy barrier

Consider the approach process for an AFM tip interacting with a surface, the net work experienced by the tip before establishing contact, W , is given by:

$$W = \int_{\infty}^{d_0} F(d)dd \quad (\text{S11})$$

where F is the measured force response as a function of tip displacement d , and d_0 is the displacement where the contact is established.

Note that the net work W is of unit of energy, and in order to quantitatively compare with the theoretically calculated energy barrier height on freestanding graphene, Φ_b , it would require the estimation of the average area for the interaction between the AFM tip and the freestanding surface, A_{avg} , following:

$$W = A_{\text{avg}}\Phi_b \quad (\text{S12})$$

To properly model A in the system of freestanding graphene, we consider a simplified picture of approach process (see Fig. S6), in which three regimes in the force response are identified. Specifically, upon reducing the separation d , the AFM tip starts probing a repulsive force, corresponding to the transition from regime I to II in Fig. S6, the repulsive force linearly increases with d , due to an increase of interaction area upon bending of graphene membrane (regime II in Fig. S6). After reaching a certain distance, where the depth is approximately equal to R_{tip} , the slope of force increase is significantly reduced (regime III). We suppose the repulsive force experienced by graphene results in a gradual stretching of graphene membrane. Given the fact that the mechanical behavior of graphene membrane dominates the force-distance response, we estimate the average area between the AFM tip and the freestanding surface throughout the approach process is approximately equal to the surface area of the hemispherical tip interacting with graphene membrane given by:

$$A_{\text{avg}} = 2\pi R_{\text{tip}}^2 \quad (\text{S13})$$

Given the tip radius characterized in SEM of 33 nm, the calculated value of Φ_b is $19\pm 5 \mu\text{J}\cdot\text{m}^{-2}$, which is nicely consistent with that predicted by our theory $20 \mu\text{J}\cdot\text{m}^{-2}$, as shown in Fig. S2.

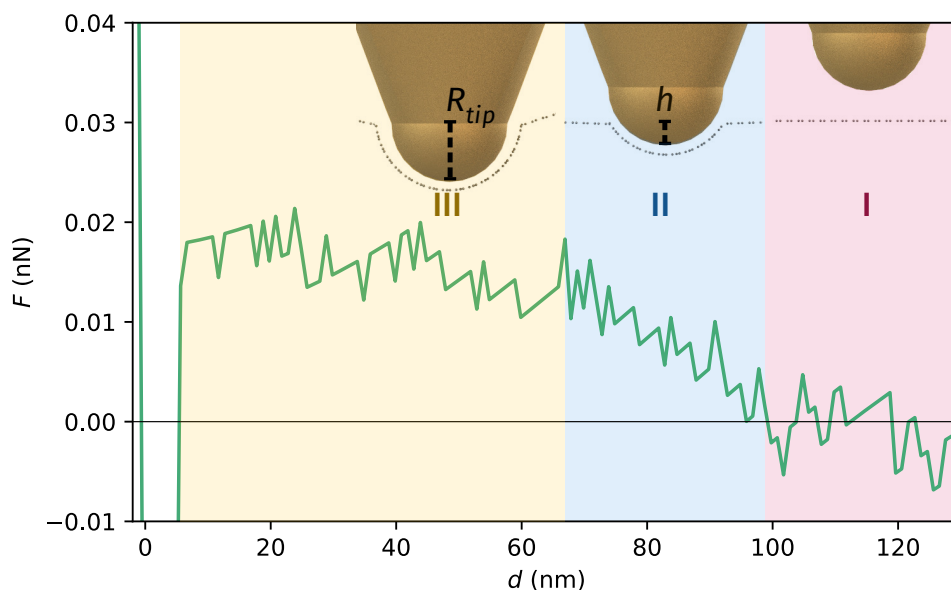


Fig. S6. **Representative force-distance response for the approach process of a gold-coated AFM tip interacting with graphene membrane.** The interaction between the AFM tip and freestanding graphene reveals three different regions, describing different force response behavior of the AFM Tip.

S4 Au epitaxy on graphene surfaces

S4.1 Relation between graphene quality and Au morphology

We have used multiple characterization techniques to examine the quality of gold deposited on freestanding graphene. As shown in Figs S7a and S7b, after the wet transfer process, >75% pores of the Quantifoil grid are covered by monolayer graphene. Raman spectroscopy (Renishaw inVia™ confocal Raman, laser 532 nm) of a typical pore (Fig. S7c) showed that the intensity ratio between the 2D and G resonance peaks (I_{2D}/I_G) is uniformly higher than 1.5 inside the pore region, indicating the successful transfer of monolayer graphene. Annealing of the wet-transferred samples under Ar/H₂ environment had minimal influence on the quality of the monolayer graphene with no significant increase of D peak intensity, as shown in Fig. S7D.

The method in this study can be used to fabricate Au nanostructures on freestanding graphene samples with varied pore size and supporting substrate. As shown in Figs S8a and S8b, similar nanostructure morphology was observed for Vac/Gr/Au with 1.2 μm and 2.0 μm pores on amorphous carbon grids, respectively. In addition, we also fabricated freestanding graphene samples suspended on perforated SiN_x chips. The SiN_x chips with pore opening ranging from 1.5~20 μm were fabricated according to Ref. [S21]. CVD-grown

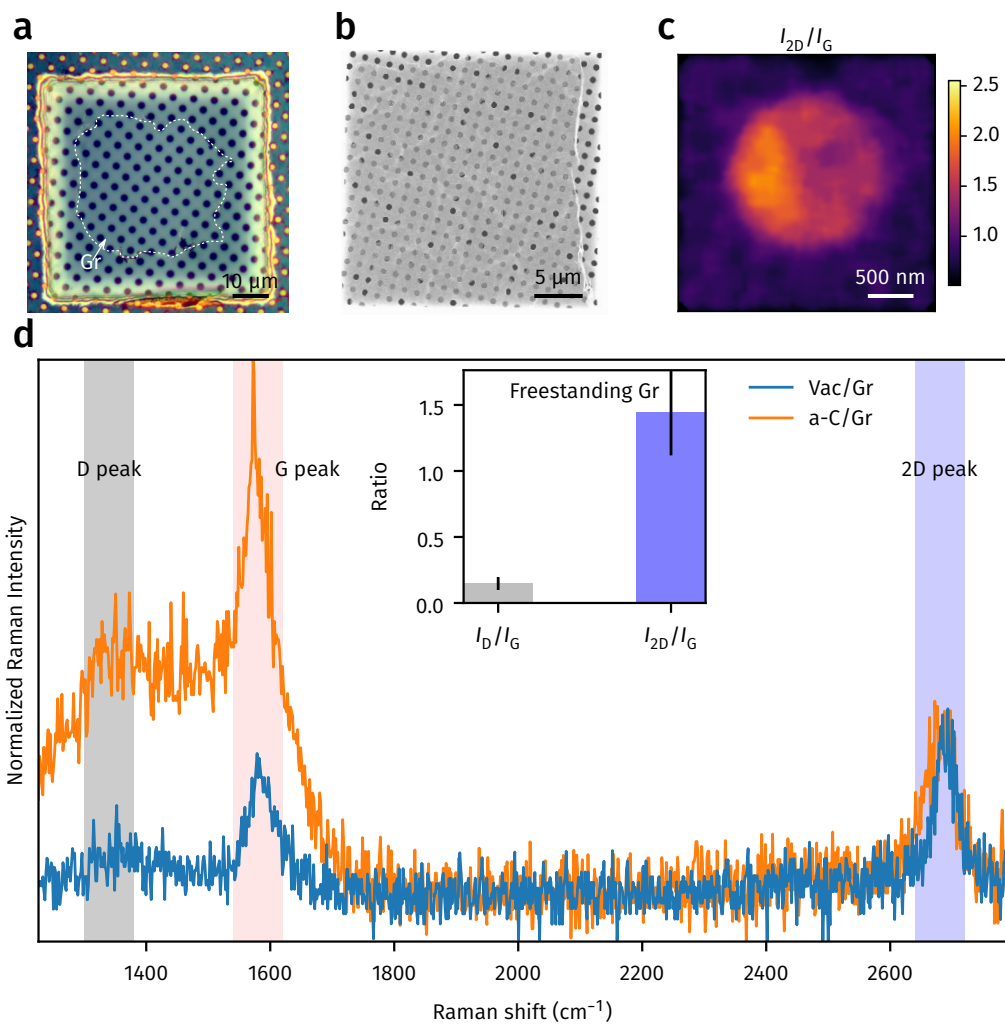


Fig. S7. Characterization of freestanding graphene fabricated by the polymer-free transfer method.

a Optical micrograph of free-standing graphene covered on Quantifoil holes. The boundary of graphene is identified by white dashed line. **b** SEM image of graphene-covered Quantifoil grid showing high yield. **c** 2D Raman mapping of the intensity ratio between 2D and G peaks near a graphene-covered hole. **d** Typical single-spot Raman spectra for freestanding graphene (blue) and graphene sitting on a-C (orange) after annealing, showing minimal influence of annealing on the defect density. The averaged I_D/I_G and I_{2D}/I_G ratio values of >50 samples are shown in the inset.

graphene coated with Poly(methyl methacrylate) (PMMA) was transferred onto the holes using standard wet-etching process^{S22}. After completely drying in ambient, the PMMA/Gr/SiN_x stack was directly annealed under Ar/H₂ environment at 600 °C to remove polymer coating. Although the radicals generated during the thermal decomposition of PMMA might bond with defective graphene surface^{S23}, as shown in Fig. S8c, at sub- μm scale, the Au nucleation density on freestanding graphene transferred on perforated SiN_x substrates is similar to the samples prepared without polymer, indicating the successful fabrication of clean graphene surfaces using both methods.

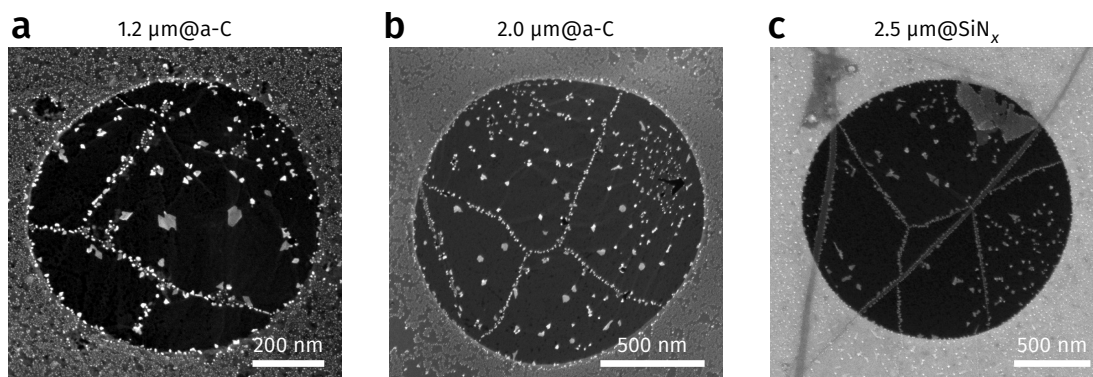


Fig. S8. **SEM images of Au deposited on graphene-covered holes on various pore sizes and substrates:** **a** 1.2 μm pore on a-C support, **b** 2.0 μm pore on a-C support, and **c** 2.5 μm pore on SiN_x support.

We also investigated the Au morphology change on freestanding and supported graphene by varying the amount of evaporation. As shown in Fig. S9, when Au evaporation increased from 2.9 $\text{ng}\cdot\text{mm}^{-2}$ to 19.5 $\text{ng}\cdot\text{mm}^{-2}$ (corresponding to nominal thickness of 0.15 nm to 1 nm, respectively), the nucleation density on the freestanding graphene remained lower than that on a-C/Gr. When $> 9.7 \text{ ng}\cdot\text{mm}^{-2}$ of Au was evaporated, coalescence of Au platelets was observed which formed larger nanostructures. It is worth noting that these interconnected platelets substantially differs the dendritic Au patterns grown on graphite surface at room temperature^{S24,S25}, which we will further explain using KMC simulations in section S4.4, as an indirect evidence of ultra-fast in-plane movement of Au on freestanding graphene.

Despite a low defect density in the CVD-grown graphene as indicated by Raman spectroscopy, atomistic defects and contamination still have strong influence on the Au deposition process. Electron micrographs in Fig. S10 demonstrate different types of high-nucleation-density Au nanostructures on defective or contaminated areas of freestanding Gr. As shown in Fig. S10a and S10b, high density Au particles were observed on mechanical defects of graphene surface, such as (i) overlayer (ii) folding and (iii) grain boundary regions,

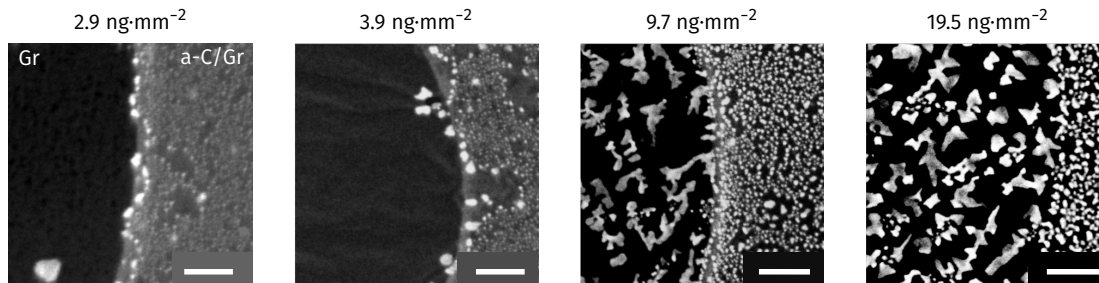


Fig. S9. **Morphology of Au nanostructures by varying amount of evaporation.** Scale bars: 100 nm.

which agrees with previous observation of metal epitaxy on graphite surface^{S26}. The high-nucleation-density areas on graphene can be linked to point and line defects, as indicated by STEM images in Fig. S10c and S10D, respectively. Au nanostructures on such defective regions usually appear as small and spherical particles surrounded by large nanoplatelets, which agrees with our hypothesis that friction of Au motion on freestanding Gr is negligible.

The correlation between surface contamination and formation of spherical Au nanostructures is further elaborated by comparing SEM images of the same graphene-covered hole in the Quantifoil grid before and after deposition of Au, as shown in Fig. S11. Our results indicate the cleanness of freestanding graphene is crucial for the observation of low-nucleation-density surface, in accordance with previous TEM studies of atomic-scale metal nucleation on graphene^{S27}.

Unlike spherical clusters observed in a-C/Gr/Au system, Au platelets in Vac/Gr/Au usually appear more regular geometries, such as hexagons or triangles. In addition to hexagonal Au platelets shown in Fig. 3D, Fig. S12 displays the STEM characteristics of a triangular Au platelet. From the FT-STEM image in Fig. S12b, in addition to the $\{\frac{4}{3}\frac{2}{3}\frac{2}{3}\}$ (and its double-spacing counterpart $\{\frac{2}{3}\frac{1}{3}\frac{1}{3}\}$) lattice planes, another set of $\{200\}$ peaks emerges, corresponding to the $\langle 001 \rangle$ zone axis perpendicular to the graphene surface. The co-existence of two sets of diffraction planes indicate the Au platelet is thicker than a few monolayers. Detailed topography profiles of these Au nanostructures were measured by atomic force microscopy (AFM) in section S4.2.

S4.2 AFM characterizations

To investigate the mechanism of 2D Au nanoplatelets formation on freestanding graphene, we performed detailed analysis of their height and size distribution on different graphene surfaces using AFM. Freestanding graphene on perforated SiN_x chips were used for all AFM experiments to overcome the issue of high surface

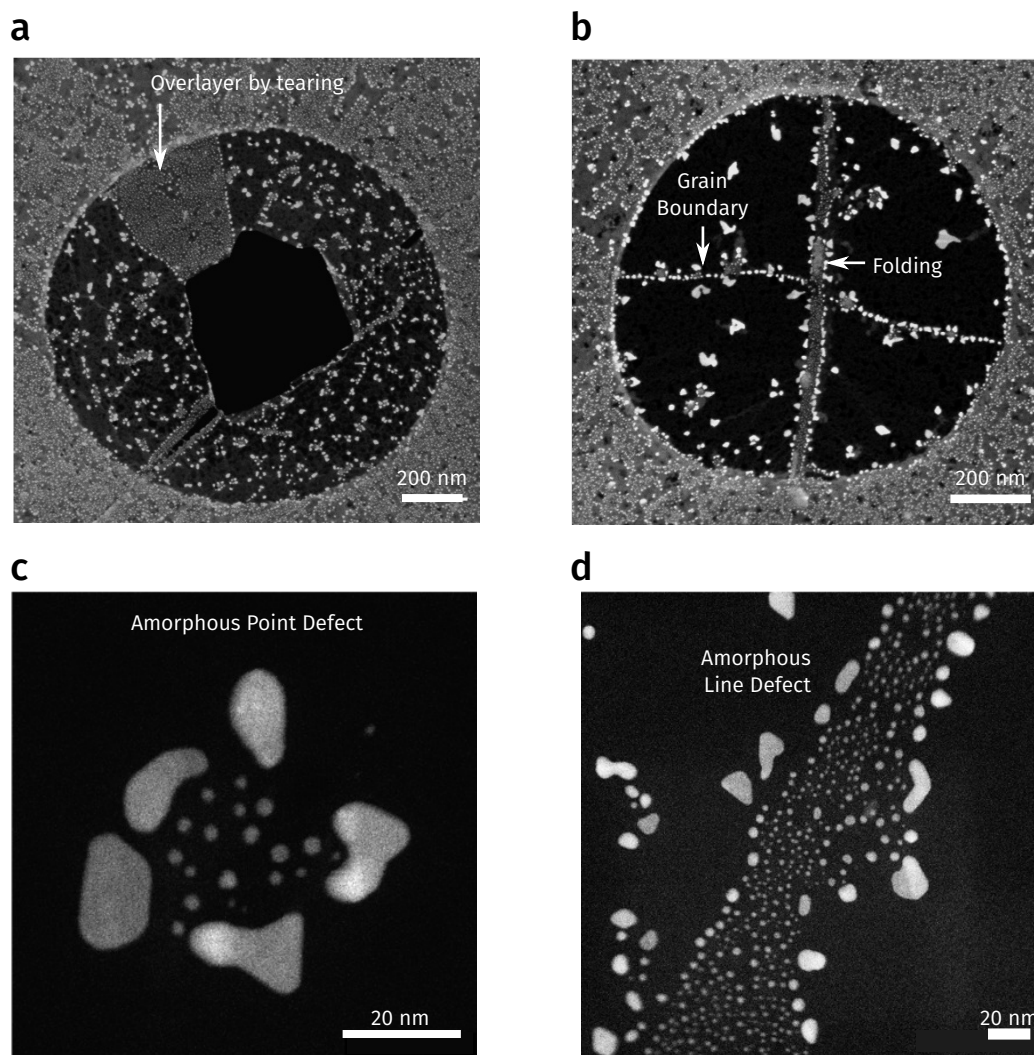


Fig. S10. **Different types of high-nucleation-density areas on freestanding graphene due to surface defects and contamination.** **a** SEM image of high-nucleation-density Au deposited on overlayer graphene formed due to tearing. **b** SEM image of high-nucleation-density Au grown near the line defect and folded regions on freestanding graphene. **c** STEM image showing the morphology of Au deposited near a point contamination site on freestanding graphene. **d** STEM image of the Au morphology near a line defect. In both cases, smaller spherical particles are formed on the contaminated area, surrounded by larger planar structures, as a result of different diffusivities on different surfaces.

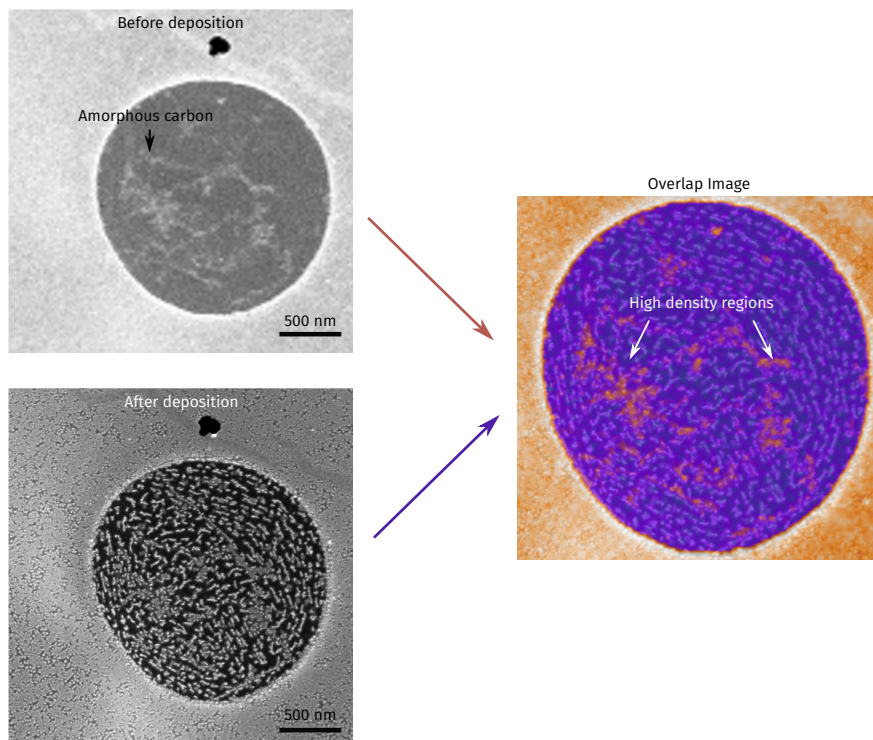


Fig. S11. **Influence of surface contamination on the Au morphology on freestanding graphene.** SEM images show that the brighter regions corresponding to amorphous carbon contamination on freestanding graphene before deposition (top left panel) coincide with the areas of high nucleation density after deposition (bottom left panel), which is confirmed by superimposing the SEM images before and after deposition (right panel).

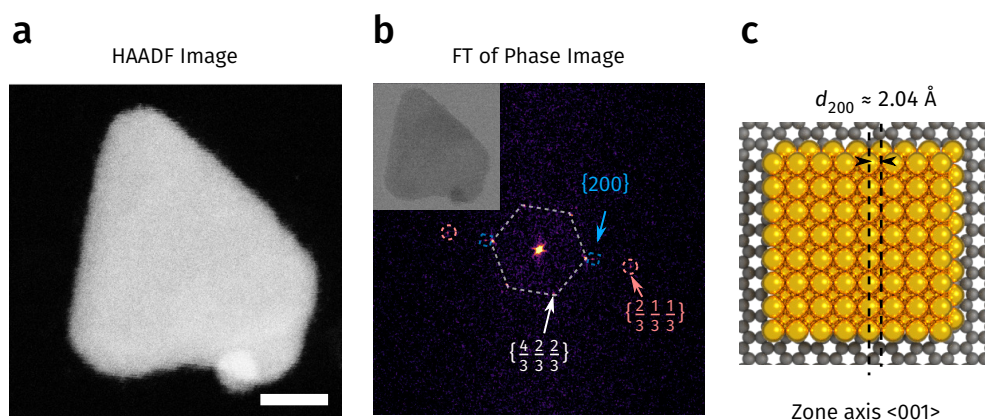


Fig. S12. **Characterization of triangular Au nanostructures.** **a** STEM image of selected triangular Au nanostructure with high-angle annular dark field (HAADF) detector. Scale bar: 5 nm. **b** Fourier-transformed (FT) image of the phase signal (inset), showing mixed lattice plane sets corresponding to $\{200\}$ (blue), $\{\frac{4}{3} \frac{2}{3} \frac{2}{3}\}$ (white) and $\{\frac{2}{3} \frac{1}{3} \frac{1}{3}\}$ (pink, double-spacing of $\{\frac{4}{3} \frac{2}{3} \frac{2}{3}\}$) families. **c** Scheme of the (200) lattice plane seen from the $\langle 001 \rangle$ zone axis of the face-center-cubic (fcc) bulk crystal of Au.

corrugation of amorphous carbon substrate after annealing. The SiN_x substrate surface remained flat after annealing. As shown in Fig. S13a, the freestanding graphene surface was highly corrugated, with height prominence at the order of 20 nm, which is corroborated by deformation mapping of the same area as shown in Fig. S13b. Despite the use of polymer coating during graphene transfer, the annealing process almost completely removed the PMMA residue, as indicated by the AFM topography in the inset of Fig. S13a.

Table S1 compares the root mean square (RMS) roughness R_q and arithmetic roughness R_a for as-prepared freestanding and substrate-supported graphene surfaces. The roughness of freestanding graphene is significantly higher than that of substrate-supported graphene, indicating the observed low nucleation density on freestanding graphene is not caused by structural superlubricity^{S24,S28} which were observed on ultraflat graphite surface.

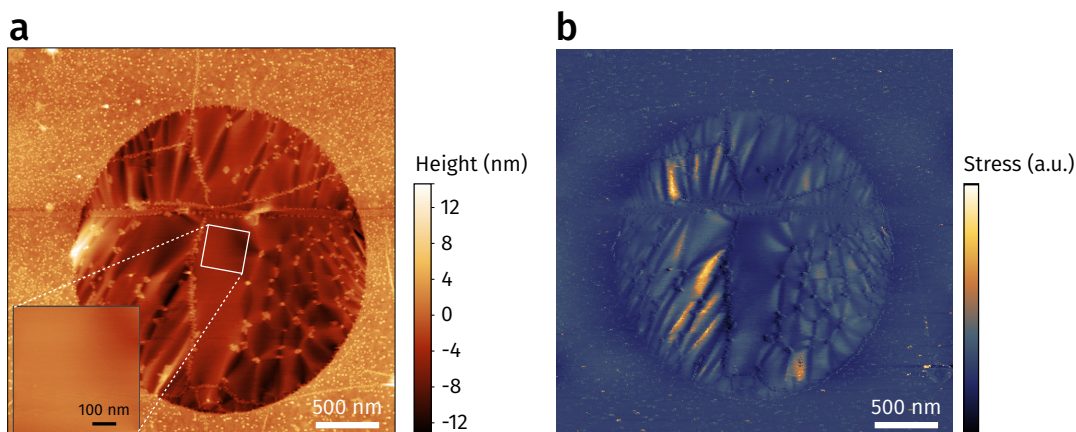


Fig. S13. **AFM topographic and stress images of a graphene-covered hole in SiN_x substrate after Au deposition.** **a** and **b** show the same mapped area with height and deformation signals, respectively. Inset of **a** shows the topography on a non-wettable region on freestanding graphene (color scale normalized for visualization).

Table S1. **Root mean square (RMS) roughness R_q and arithmetic roughness R_a of different graphene surfaces after annealing.** The mean roughness of freestanding graphene is substantially higher than the substrate-supported graphene surfaces due to high degree of wrinkle and surface corrugation.

	Freestanding Gr	a-C/Gr	SiN_x/Gr	SiO_2/Gr
RMS Roughness R_q (nm)	2.15 ± 0.61	0.663 ± 0.029	0.409 ± 0.042	0.242 ± 0.019
Arithmetic Roughness R_a (nm)	1.70 ± 0.45	0.450 ± 0.015	0.324 ± 0.028	0.195 ± 0.011

Using AFM, we were also able to identify the influence of thermal annealing by comparing the topography of the same region before and after thermal treatment. Fig. S14a shows the AFM topography of Vac/Gr/Au

directly after Au evaporation with large non-wettable area. However, after placing the sample under ambient conditions for 1 day, significant contamination layer with average height of $1 \sim 2$ nm was observed on the previously clean regions (Fig. S14b and inset). Such airborne contaminants resembles those in a recent report^{S29}, and their average height is distinguishable from the evaporated Au nanostructures. Interestingly, after re-annealing the sample under Ar/H₂ environment, the contaminants completely removed (Fig. S14c). The comparison clearly indicates thermal annealing of graphene sample prior to the Au evaporation is the key to obtain clean and non-wettable freestanding graphene surface, as the hydrocarbon contaminants are known to promote metal nucleation on graphitic surfaces^{S27,S30,S31}. We also found that one Au particle on

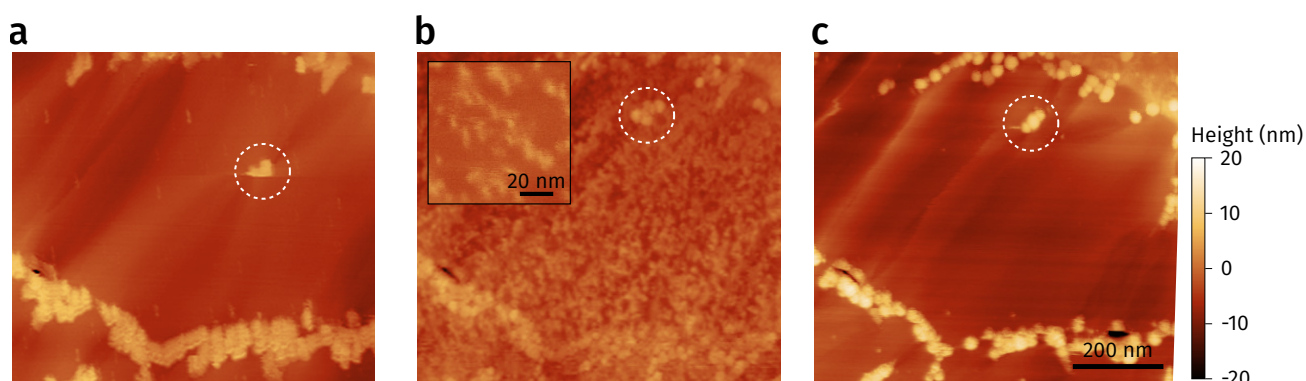


Fig. S14. Effect of thermal annealing on the quality of freestanding graphene and Au nanostructure. **a** AFM topography of Vac/Gr/Au directly after Au deposition. **b** AFM topography of same area after the sample was kept in ambient for 24 hours. Airborne contamination can clearly be observed. Inset: zoomed-in mapping on the contaminated area. **c** The same area after re-annealing the sample at 600 °C. The amorphous contaminants were completely removed, while the average height of Au nanostructures increases. Note the Au nanostructure marked in white circle appeared to be moved from **a** to **c**.

the freestanding graphene surface (marked in white circle, Fig. S14a-c) had apparent lateral displacement before and after the thermal treatment. On the contrary, although the shape and height changed after thermal annealing, Au nanostructures near line defects and on SiN_x/Gr surface showed negligible movement. We therefore conclude that on freestanding graphene, Au nanostructures with lateral length up to tens of nanometers could still have considerable high mobility and low friction.

The movement of Au nanostructures could also be induced by external mechanical force. As shown in Fig. S15, during continuous AFM scanning in ambient, the triangular Au platelet (marked in white dashed lines) showed significant lateral displacement (> 2 times of its size). However, such displacement was not observed for Au clusters evaporated on line defects or substrate-supported graphene. Consider the huge

difference between the lateral size of Au platelet (> 50 nm) and the apex of AFM tip (ScanAsys Air, ~ 2 nm), it is unlikely that such displacement was caused by pickup and re-deposition by the AFM tip^{S32}.

The tip-induced motion of Au platelets can be explained by the reduction of equilibrium Gr-Au interaction potential caused by the many-body repulsive interaction. Following our analysis in section S2.3, the attractive potential of Vac/Gr/Au system is significantly reduced compared with the Sub/Gr/Au system when d is close to the vdW contact distance (Fig. S3). Similarly, on defective area, we expect the attractive potential to be also large due to the strong adhesion between defective graphene and Au^{S27}. As a result, interaction between the AFM tip and the Au platelet on freestanding graphene can easily overcome the attractive potential between Au and graphene, leading to considerable lateral displacement.

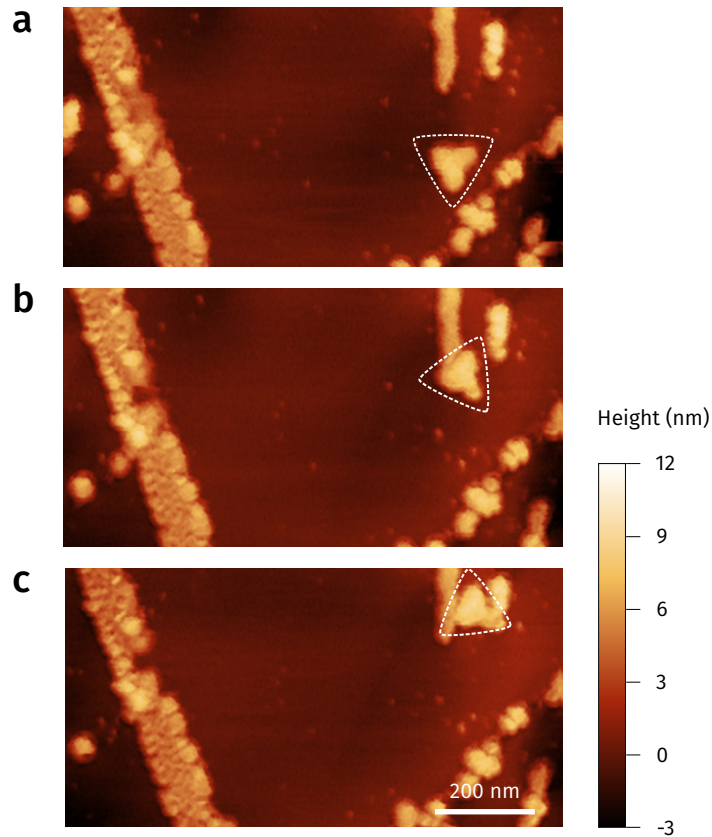


Fig. S15. **Observation of Au nanostructure displacement during AFM measurement in ambient.** **a, b** and **c** are consecutive AFM images of Au nanostructure on freestanding graphene surface taken during continuous scanning. A triangular nanoplatelet on freestanding graphene appeared to move >200 nm (>2 times the lateral size of Au platelet) induced by the motion of AFM tip. On the other hand, no apparent change of morphology was observed for Au deposited on line defects. The results indicate that the friction between freestanding graphene and Au nanostructures with lateral size > 50 nm is still considerably small.

S4.3 Discussion about mechanism

More details about the mechanism of 2D Au platelets formation on freestanding graphene are discussed as follows. First we rule out the possibility that larger Au structure formation was due to that Au is easier to wet freestanding graphene. As shown in Fig. S16, if such thermodynamic hypothesis is correct, it is more energetically favorable for the Au clusters to be adsorbed on freestanding graphene than the separated system. In other words, $\Delta G_{\text{ad}} < \Delta G_{\text{sep}}$ is expected, where ΔG_{ad} and ΔG_{sep} are the free energy of adsorbed and separated systems, respectively. Assume the surface area of graphene is A_{Gr} , the surface area of isolated Au is A_{Au} , and the fraction of Au-covered graphene surface is f , we have:

$$\Delta G_{\text{sep}} = A_{\text{Gr}}\gamma_{\text{Gr}} + A_{\text{Au}}\gamma_{\text{Au}} + \Delta G_{\text{co}} \quad (\text{S14})$$

$$\Delta G_{\text{ad}} = A_{\text{Gr}}(1-f)\gamma_{\text{Gr}} + A_{\text{Gr}}f\gamma_{\text{Au-Gr}} + A_{\text{Gr}}f\gamma_{\text{Au}} + \Delta G_{\text{co}}$$

where γ_{Au} and γ_{Gr} are the surface energy of Au and freestanding graphene, respectively, $\gamma_{\text{Au-Gr}}$ is the interfacial energy between Au and graphene, and ΔG_{co} is the free energy of cohesion (chemical bonding). Consider the fact $A_{\text{Gr}} \gg A_{\text{Au}}$, the inequality $\Delta G_{\text{ad}} < \Delta G_{\text{sep}}$ can be approximated by

$$\gamma_{\text{Au}} + \gamma_{\text{Au-Gr}} < \gamma_{\text{Gr}} \quad (\text{S15})$$

Since $\gamma_{\text{Au}} \gg \gamma_{\text{Gr}}$, $\gamma_{\text{Au-Gr}}$ must be negative. Combine with $\gamma_{\text{Au-Gr}} = \gamma_{\text{Gr}} + \gamma_{\text{Au}} - \Delta W_{\text{Au-Gr}}$, where $\Delta W_{\text{Au-Gr}}$ is the work of adhesion between graphene and Au, $\Delta W_{\text{Au-Gr}}$ should be considerably high to allow the wetting of Au on freestanding graphene to occur. This is nonphysical since i) attractive vdW potential is stronger with substrate-supported graphene, following the discussion in section S2.3 and ii) stronger adhesion leads to higher nucleation density, contradictory to our experimental findings.

To further study the formation of large 2D platelets on freestanding graphene, we performed statistic analysis for the Au nanostructures grown on different graphene surfaces using both AFM topography and SEM micrograph. As shown in Fig. S18, the Au nucleation density measured by AFM ranks $\text{Vac/Gr} < \text{SiO}_2/\text{Gr} < \text{SiN}_x/\text{Gr} < \text{a-C/Gr}$, which agrees with our SEM images in Fig. 3e. Fig. S18 compares the AFM height distribution of Au nanostructures from > 500 samples points per graphene surface measured. The fitted distribution curves indicate that the height of Au nanostructures follows $\text{Vac/Gr} > \text{SiO}_2/\text{Gr} \approx \text{SiN}_x/\text{Gr} > \text{a-C/Gr}$. In other words, Vac/Gr is actually slightly *less wettable* to Au than the substrate-supported graphene

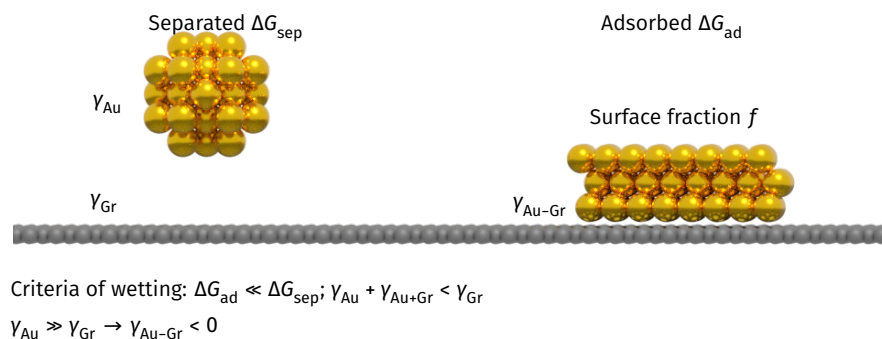


Fig. S16. **Thermodynamic considerations of a 2D platelet formed on freestanding graphene.** Wetting of high-surface-energy Au on Gr indicates the free energy of adsorbed system ΔG_{ad} should be smaller than in the separated system ΔG_{sep} , which in turn means the interfacial tension $\gamma_{\text{Au-Gr}}$ is negative and adhesion between Au and Gr increases. This contradicts to the experimental observation of ultra-low condensation of Au on freestanding graphene.

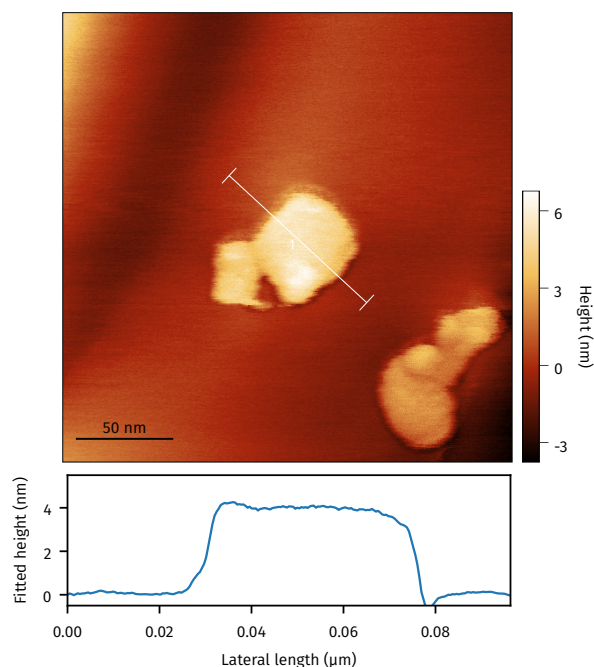


Fig. S17. **Direct AFM height measurement of a typical Au platelets on freestanding graphene.** The height profile is flattened using polynomial background regression, showing a platelet height of 3.90 ± 0.1 nm.

surfaces, in particular a-C/Gr, which agrees with our analysis in Fig. S3. On the other hand, the average particle area for Vac/Gr/Au increases by $> 10^2$ times compared with that for a-C/Gr/Au, as shown in Fig. S18c. Notably, the distribution of particle area for Vac/Gr/Au has an tail towards 10^4 nm². In combination with the observation of low friction interface between Vac/Gr and Au (Fig. S15), we conclude that the formation of larger 2D crystals on freestanding graphene, can only be ascribed to kinetic effects. In fact, such 2D platelet formation may be metastable, as we observed the height of Au nanostructures on freestanding graphene increased from ~ 6 nm (as prepared, Fig. S14a) to ~ 14 nm after annealing at 600 °C (Fig. S14c), further proving that the freestanding graphene is poorly wettable by Au.

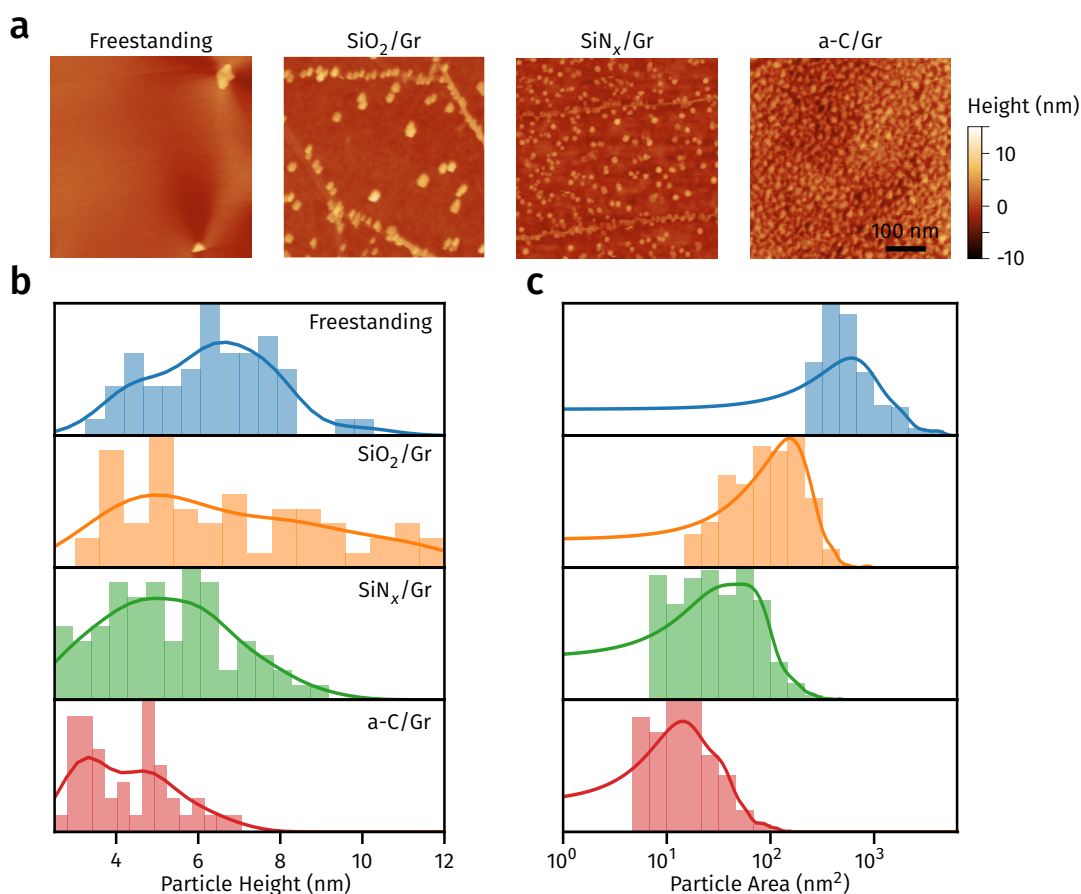


Fig. S18. **Statistics of Au nanostructures grown on freestanding or substrate-supported graphene surfaces.** **a.** AFM topography of Au deposited on freestanding graphene and graphene supported by SiO₂, SiN_x and a-C substrates. **b** and **c.** Height and surface area distribution of Au particles on different graphene interfaces, respectively. The solid line in **b** and **c** are the continuous distribution function fitted using Gaussian kernel. Au nanoparticles on freestanding graphene are slightly higher while much larger in lateral size compared with those on substrate-supported graphene. The statistics were based on both AFM and SEM measurements.

To estimate the surface diffusivity D of Au on different graphene surfaces, we compared the nucleation density N_{nu} measured by SEM images as shown in Fig. S19 insets. The ratios D_{fs}^*/D_i^* between the effective diffusivities on freestanding graphene (D_{fs}^*) and graphene surface i (D_i^*) calculated using the relation $N_{\text{nu}} \propto (D^*)^{-1/3}$, are also plotted. The effective diffusivity on freestanding graphene can be up to 10^9 times faster than that on a-C/Gr. Furthermore, although the average particle area on Vac/Gr/Au is larger than that of substrate-supported graphene, the low nucleation density leads to less amount of Au deposited on Vac/Gr surface, as a result of the existence of repulsive vdW interaction.

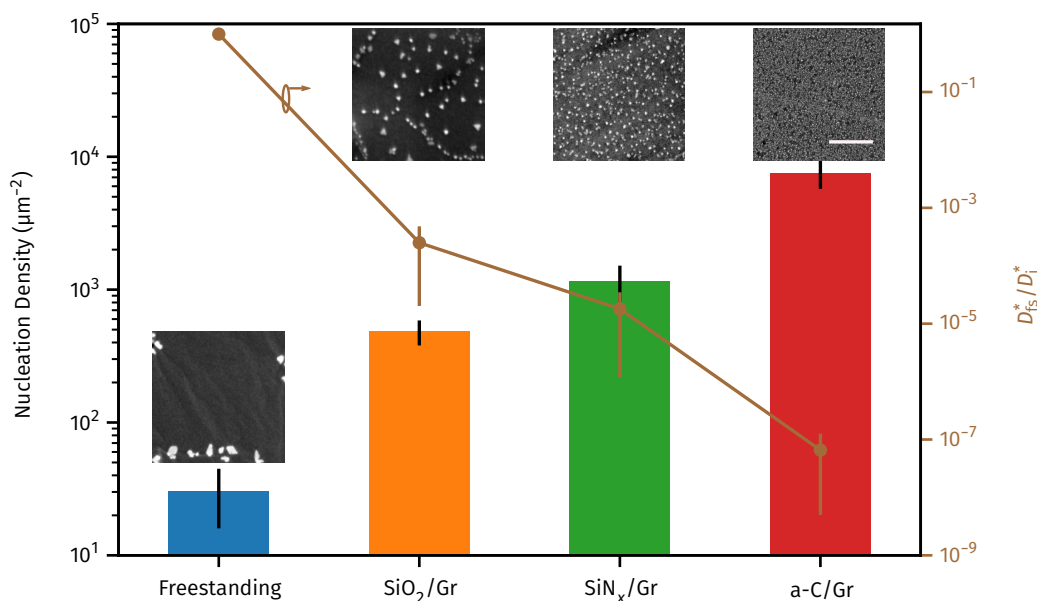


Fig. S19. **Histograms of nucleation density (left vertical axis) and corresponding SEM images of Au morphology on graphene with different substrates.** The calculated ratio D_{fs}^*/D_i^* between effective surface diffusivities of freestanding graphene (D_{fs}^*) and graphene supported by substrate i (D_i^*) are shown as the right vertical axis. Scale bars of SEM insets: 200 nm.

To rule out the possibility that the variation of Au nucleation density is influenced by the defects of the CVD-grown graphene, we also measured Au morphology on mechanically-exfoliated graphene. Monolayer (ML) graphene mechanically exfoliated onto SiO₂ substrate was identified by optical micrograph (Fig. S20a). As shown in Fig. S20b-d, the nucleation density, morphology and height distributions of Au deposited onto mechanically-exfoliated graphene are similar to those observed in SiO₂/Gr/Au samples prepared using CVD-grown graphene.

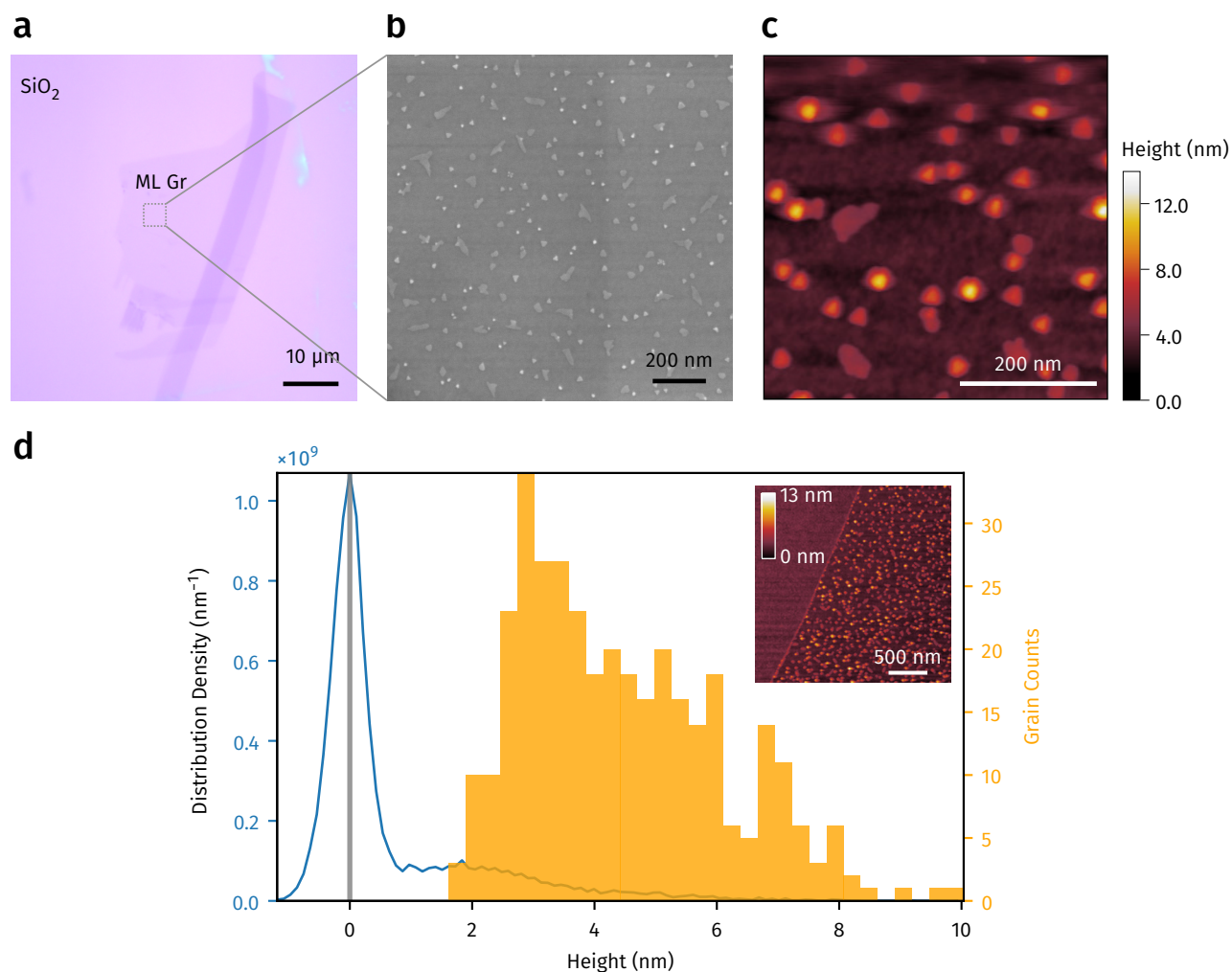


Fig. S20. **Au nanostructures deposited on mechanically-exfoliated substrate-supported graphene.** **a** Optical image of a piece of exfoliated graphene transferred onto SiO₂ substrate. Monolayer (ML) regions are identified by optical contrast. **b** and **c** SEM and AFM characterizations of Au nanostructures on freestanding Gr when the nominal deposition thickness is 0.1 nm, respectively. Despite the clean graphene surface created by mechanical exfoliation, nucleation density of Au clusters is still higher than on freestanding Gr (Fig. 3D). **d**. Left axis: height distribution density of all pixels in the inset AFM image, the reference level of the substrate (0 nm) is taken as the center of the first peak. Right axis: histogram of average height per Au nanoplatelet in the inset AFM image, showing similar trend with Fig. S18c.

S4.4 KMC simulations of Au diffusion

The detailed kinetic processes and their corresponding activation energy barriers in the KMC simulations are schematically shown in Fig. S21. The KMC simulation box was implemented on a $m \times n \times 2$ triangular mesh with periodic boundary conditions (PBC), as shown in Fig. S22. To simulate the experimental conditions on the CVD-grown graphene, we implemented line and point defects on top of the triangular meshes (Fig. S22a, pink dots) by assigning higher diffusion barrier ΔE_d^* . Practically, when simulating very fast Au diffusion on freestanding graphene, such defective regions act as preferential nucleation sites to promote growth of larger Au platelets. A typical snapshot of the KMC simulation can be seen in Fig. S22b.

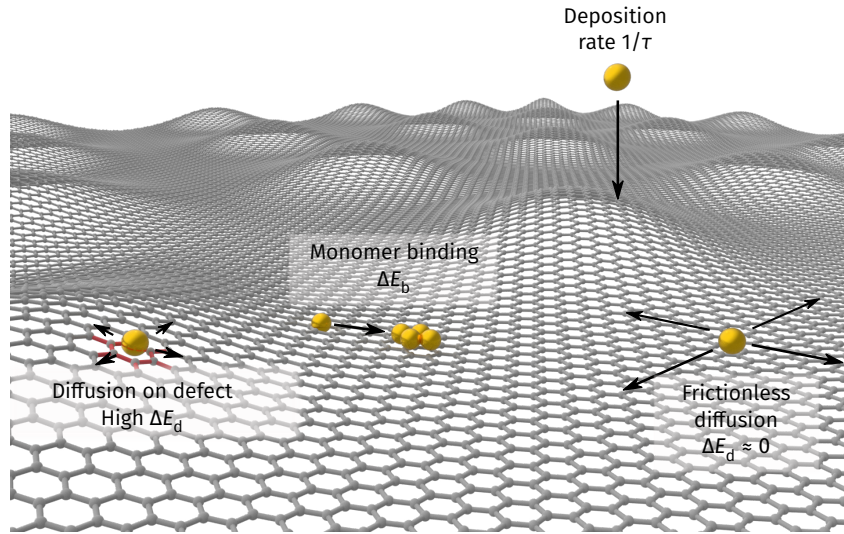


Fig. S21. **Scheme of different kinetic processes for the Au deposited on freestanding Gr.** The Au atoms are deposited onto the freestanding Gr surface with a rate of $1/\tau$, where τ is the characteristic time interval of incoming Au atoms. On pristine Gr interface, the diffusion energy barrier ΔE_d is nearly negligible, leading to friction-less diffusion, while on defective / contaminated area ΔE_d is much higher. On the other hand, Au atoms are bonded to form covalent structures with a energy barrier of ΔE_b . The formation of large 2D Au structures are enabled when ΔE_d on pristine freestanding Gr is even much lower than ΔE_b .

The Au evaporation process is modeled as follows. The rate of deposition is defined as $\nu = 1/\tau$, where τ is the characteristic time scale between two deposition events, which follows:

$$\nu = J_e N_{\text{site}} = \nu_0 \exp\left(-\frac{\Delta E_e}{k_B T}\right) \quad (\text{S16})$$

where J_e is the flux of evaporation (measured in $\text{ML} \cdot \text{s}^{-1}$), N_{site} is the density of lattice sites in the KMC

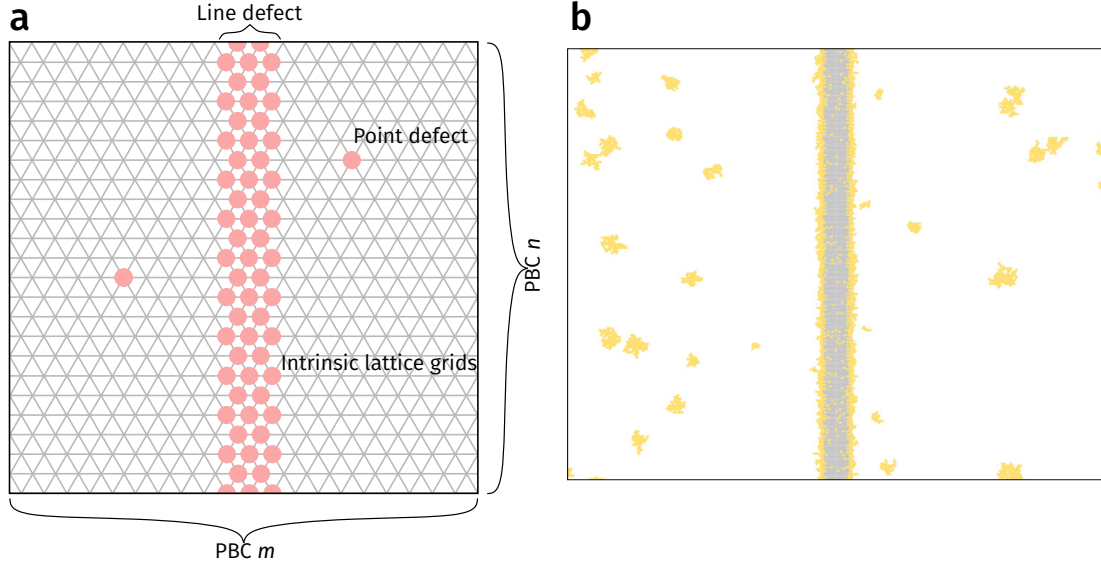


Fig. S22. **Schematic diagram of simulation box used in our 2D lattice-KMC.** **a** The simulation box consists of $m \times n \times 2$ triangle grids on which Au atoms are allowed to move. Line and point defects (pink dots) are implemented by assigning higher ΔE_d value onto corresponding grid points. **b** Snapshot of a KMC simulation containing line defects. Yellow dots represents Au.

simulation, ν_0 is the rate prefactor, and ΔE_e is the effective energy barrier for the evaporation process. For $J_e = 0.01 \text{ ML}\cdot\text{s}^{-1}$, $m = n = 100$ and $\nu_0 = 10^{10} \text{ s}^{-1}$, we have $\Delta E_e \approx 15k_B T$. We also note in the current KMC framework, the difference between freestanding and substrate-supported graphene is reflected by the choice of ΔE_d^0 , and surface corrugation is not taken into account.

There are several simplifications used in the KMC simulations. First, we do not specify whether the Au on each mesh grid is a single atom or a cluster. As a result, the binding between two Au units may be slower than that of surface diffusion. To simplify the simulation, the Au units are not allowed to move after coalescence occurs. Moreover, since in this study we do not care about absolute time scale of cluster formation, the exact value for ν_0 does not affect the final result.

The morphology of Au nanostructures are majorly influenced by the following factors: i) magnitude of ΔE_e and ii) competition between ΔE_d and ΔE_b . For all simulations we fix the diffusion barrier on defects ΔE_d^* to $15 k_B T$.

Influence of ΔE_e Fig. S23 compares the different snapshots of Au nanostructures by varying ΔE_e (horizontal direction) and ΔE_d^0 (vertical direction). Independent of the in-plane diffusion rate, by lowering ΔE_e (faster deposition), the nucleation density of Au nanostructures always increases. This is because when in-

creasing the evaporation rate, there are more mobile Au on the graphene surface at the same time, leading to higher rate of coalescence. In the experiment of Au evaporation, it is therefore always favorable to use lower deposition rate for the formation of sparse and large clusters on freestanding graphene.

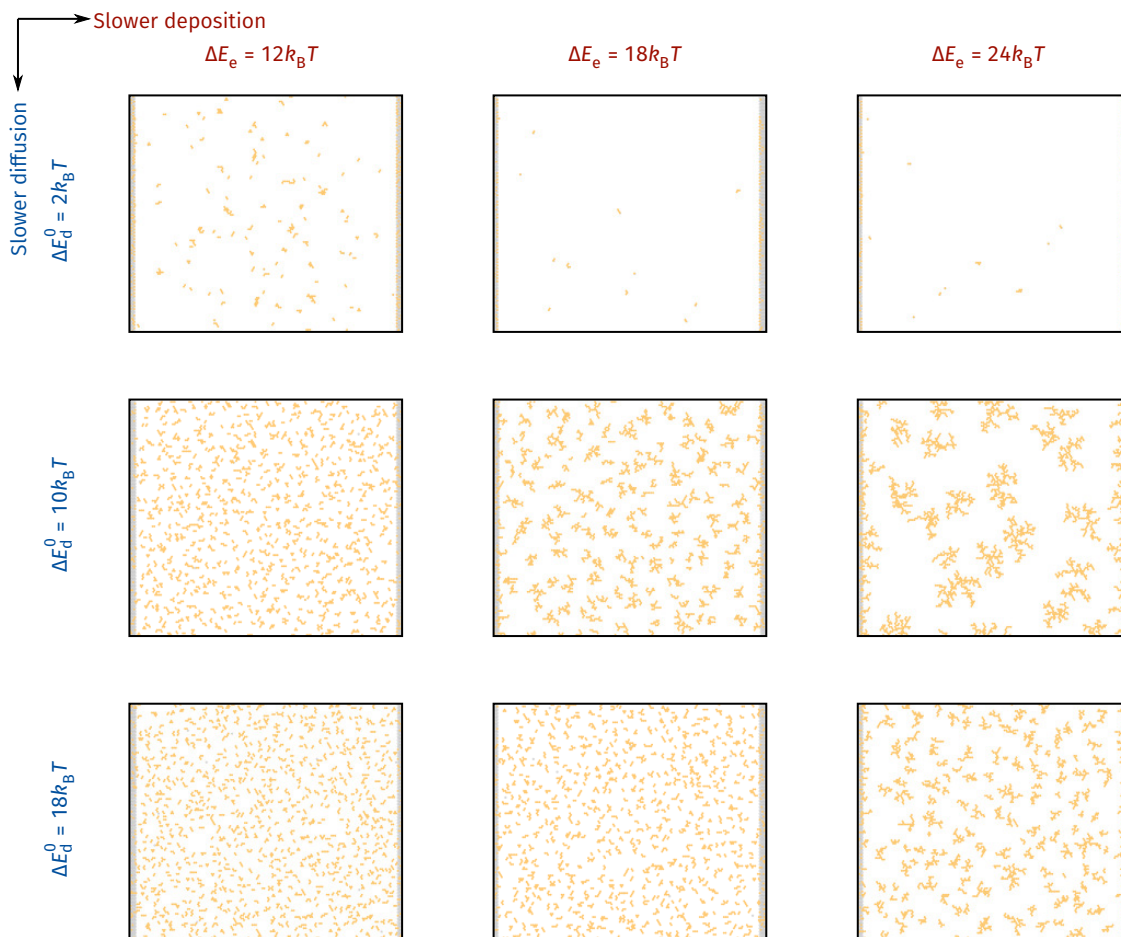


Fig. S23. **Snapshots of Au nanostructure formation at 10^6 time steps by varying ΔE_e and ΔE_d^0 .** Independent of ΔE_d^0 , decreasing ΔE_e always leads to higher nucleation density. The value of ΔE_b is $10k_B T$ for all simulations. The line defects are plot at the edge of the simulation box for illustration purpose. Note for very fast diffusion cases, the time scale of individual cluster to grow appears to be longer than 10^6 steps, leading to smaller cluster size.

Influence of ΔE_d^0 and ΔE_b The influence of ΔE_d^0 and ΔE_b on the Au nanostructure formation is more complex. As shown in Fig. S24, with a lower $\Delta E_d^0/\Delta E_b$ ratio, the nucleation density of Au nanostructures decreases. On the other hand, we also observe that at same $\Delta E_d^0/\Delta E_b$ ratio, increasing ΔE_d^0 leads to formation of higher degree of nucleation. In both scenarios, the increasing of nucleation density can be explained

by shorter time scale for Au coalescence to occur.

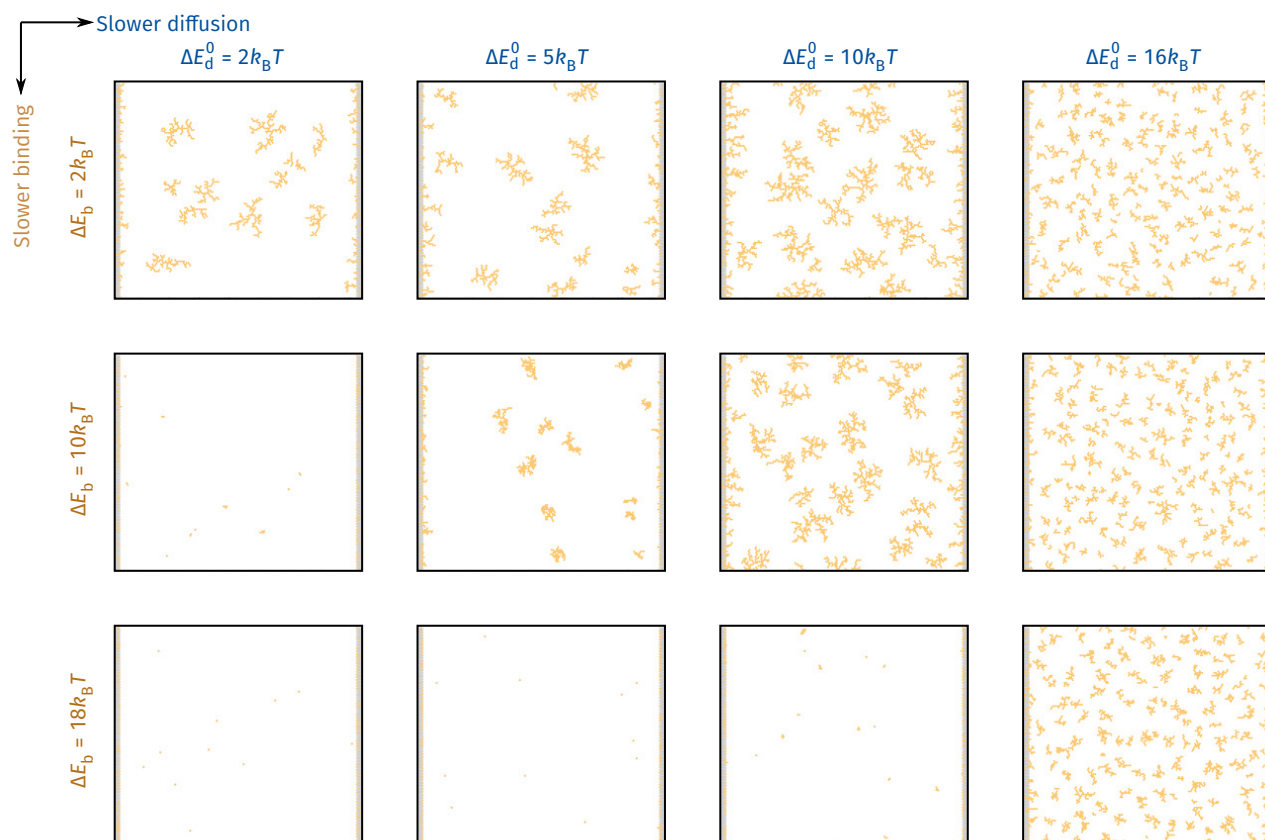


Fig. S24. **Snapshots of Au nanostructure formation at 10^6 time steps by varying ΔE_b and ΔE_d^0 .** Different $\Delta E_b^0/\Delta E_d$ ratios lead to distinct morphology and nucleation density of Au nanostructures. The value of ΔE_e is $20k_B T$ for all simulations. The line defects are plot at the edge of the simulation box for illustration purpose. Note for very fast diffusion cases, the time scale of individual cluster to grow appears to be longer than 10^6 steps, leading to smaller cluster size.

The $\Delta E_d^0/\Delta E_b$ ratio also influences the morphology of individual Au nanostructure. A general trend observed in Fig. S24 is that for higher $\Delta E_d^0/\Delta E_b$ value, the Au nanostructure tends to dendritic, while for lower $\Delta E_d^0/\Delta E_b$ value the Au nanostructures becomes more compact. This can be explained by the fact that when the rate of binding and diffusion are comparable, the structure formed is not fully relaxed. We use this feature to explain the distinct Au morphology observed on bulk graphite and freestanding graphene surfaces, as shown in Fig. S25. Although the nucleation density of Graphite/Au (Fig. S25a) at room temperature is comparable with that of Vac/Graphene/au (Fig. S25b), the dendritic pattern formation on Graphite/Au indicates the in-plane diffusion of Au is faster on freestanding graphene, given the fact that the Au-Au coalescence rate is almost independent on the substrate^{S33,S34}. On the other hand, previous studies showed

that hexagonal/triangular Au nanostructures on graphite could only be formed during high-temperature deposition^{S25,S30,S31}, indicating that ΔE_d^0 on freestanding graphene is lower than of bulk graphite. Taking the surface corrugation of freestanding graphene into account, the fast in-plane Au diffusion on freestanding graphene beyond the structural superlubricity, can only be explained by the existence of manybody repulsive vdW interactions.

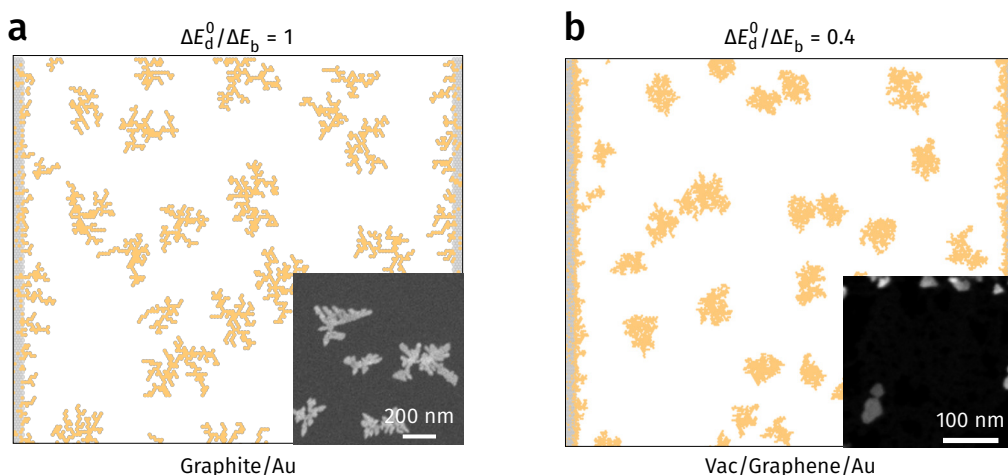


Fig. S25. **Simulated morphology of Au nanostructures on bulk graphite (a) and freestanding graphene (b) surfaces.** The dendritic patterns on graphite are formed as a result of the high $\Delta E_d^0/\Delta E_b$ ratio, while hexagonal and triangular structures are observed on freestanding graphene due to lower $\Delta E_d^0/\Delta E_b$. Experimental SEM images for Graphite/Au and Vac/Graphene/Au fabricated from Au evaporation at room temperature are shown as insets of **a** and **b**, respectively.

S5 Molecular epitaxy of BPE molecules

S5.1 Practical considerations

Molecular epitaxy on graphene surface is known to be influenced by the doping state of graphene^{S35}. To rule out the possibility that observed polymorphism of BPE was due to doping, Raman spectroscopy was used to monitor the charge density of graphene transferred on as-cleaned SiO₂ (SiO₂/Gr), self-assembled octadecyltrichlorosilane (OTS) on SiO₂ (OTS/Gr) and gold (Au/Gr). The OTS-SiO₂ substrate was used as a reference for suppressing potential substrate-induced doping^{S36}. As shown in Fig. S26, on all substrates the 2D peak is higher than the G peak, and D peak intensity is negligible. As summarized in Table S2, the 2D and G peak positions of SiO₂/Gr and Au/Gr samples are statistically similar. From literature^{S37}, the positions of the G-peak for SiO₂/Gr and Au/Gr indicates both samples have doping density less than $2 \times 10^{12} e\text{-cm}^{-2}$.

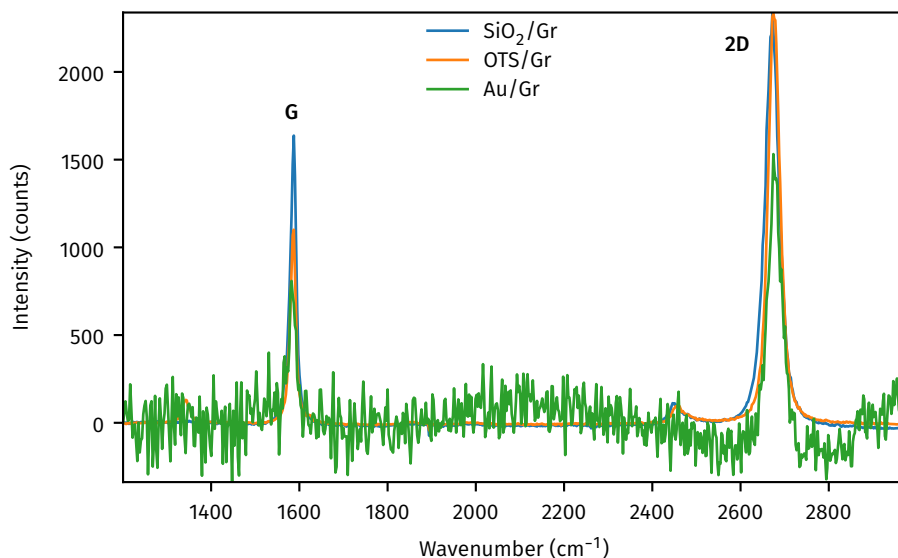


Fig. S26. **Typical Raman spectra of monolayer graphene transferred onto as-cleaned SiO₂ (SiO₂/Gr), OTS-treated SiO₂ (OTS/Gr) and gold (Au/Gr) substrates.** Raman spectra were taken using 532 nm laser. In all cases the 2D peak remains higher than G peak indicating monolayer graphene. The positions of 2D and G peaks do not have apparent shift, similar doping densities in these substrates.

Table S2. **Peak position and full width at half-maximum (FWHM) of G and 2D peaks in the Raman spectra in Fig. S26.** Statistical average and deviation are taken from over 80 data points. The peak parameters are fitted using Gaussian function.

Substrate	Position G (cm ⁻¹)	FWHM G (cm ⁻¹)	Position 2D (cm ⁻¹)	FWHM 2D (cm ⁻¹)
SiO ₂ /Gr	1585.69 ± 2.69	8.33 ± 2.30	2675.62 ± 4.15	17.75 ± 2.52
OTS/Gr	1584.76 ± 1.07	8.07 ± 1.48	2676.42 ± 2.57	16.05 ± 3.16
Au/Gr	1582.50 ± 2.48	10.31 ± 2.93	2676.25 ± 3.43	18.80 ± 2.05

S5.2 Determining crystallographic parameters

The processes for determining the crystallographic parameters (crystal lattice constant and interplanar distances) are described as follows. The full-range GIWAXS spectra for SiO₂/Gr/BPE and Au/Gr/BPE are shown in Fig. S27. A rectangular beam stop was used to reduced the scattering from the substrate. The 1D diffraction profile was generated by first subtracting the background from the 2D GIWAXS spectra using rolling-ball algorithm^{S38}, and calculated using:

$$I_{1D}(q) = \int_0^{\pi/2} I_{2D}(q, \theta) q d\theta \quad (\text{S17})$$

where I_{2D} and I_{1D} are the 2D and 1D X-ray diffraction intensity, $q = |\mathbf{q}|$ is magnitude of the diffraction wave vector, and $\theta = \arctan \left| \frac{q_z}{q_{xy}} \right|$.

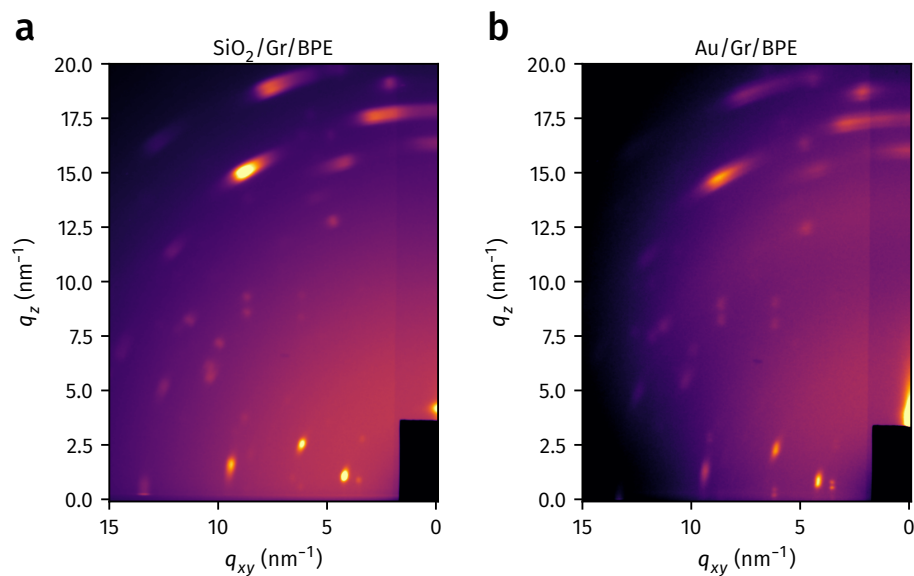


Fig. S27. Full-range GIWAXS spectra of SiO₂/Gr/BPE **a.** and Au/Gr/BPE **(B)** systems corresponding to Fig. 4c

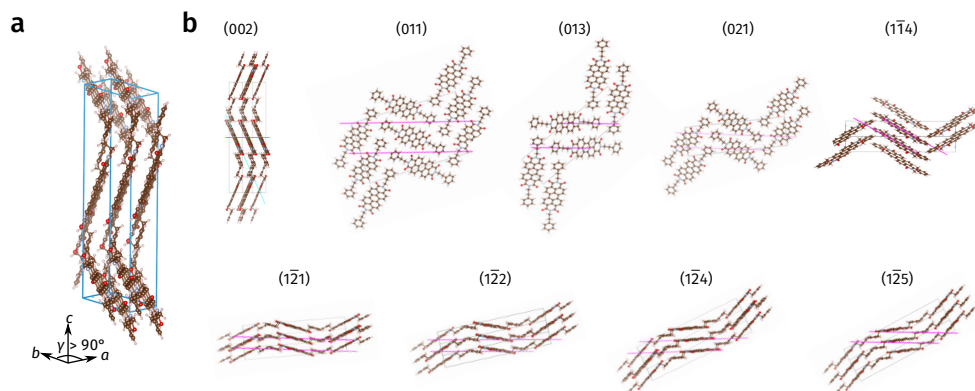


Fig. S28. **Lattice structure of BPE.** **a.** Schematic of BPE unit cell with monoclinic symmetry. **b.** Typical lattice planes in BPE single crystal with corresponding (hkl) indices.

Single crystal data of BPE molecule from literature^{S39} (CCDC DICNIM01) were used as a reference for assigning the Miller indices for the lattice planes. As shown in Fig. S28a, the unit cell of BPE single crystal is monoclinic with $\gamma \neq 90^\circ$. The major diffraction planes are shown in Fig. S28b. The high- q (short interplanar distance) diffraction planes $(1\bar{1}4)$, $(1\bar{2}1)$, $(1\bar{2}2)$, $(1\bar{2}4)$ and $(1\bar{2}5)$ are associated with the PTCDI basal plane of BPE molecule. The simulated 1D X-ray diffraction profile from BPE single crystal data is shown in Fig. S29

(black line). In comparison, Fig. S29 also show the experimental 1D X-ray diffraction profiles for sublimed BPE powder (blue line), SiO₂/Gr/BPE (orange line) and Au/Gr/BPE (green line). The diffraction peaks in the experimental 1D X-ray diffraction profiles were assigned as follows. Assuming the BPE molecules in the experimental samples remained the monoclinic lattice structure, we first guessed the Miller indices for the most prominent peaks in each 1D profile using the reference data from BPE single crystal. The lattice constants a , b , c , γ were then calculated using least-square fitting based on the equation of interplanar spacing in a monoclinic unit cell^{S40}:

$$\frac{1}{d_{hkl}^2} = \frac{1}{\sin^2 \gamma} \left[\frac{h^2}{a^2} + \frac{k^2}{b^2} + \frac{l^2 \sin^2 \gamma}{c^2} - \frac{2hk \cos \gamma}{ab} \right] \quad (\text{S18})$$

where $d_{hkl} = 2\pi(q_{hkl})^{-1}$ is the interplanar distance. The assignment of Miller indices was refined iteratively until the mismatches between experimental and the fitted values d_{hkl} were minimized. The peak assignment for BPE powder, SiO₂/Gr/BPE and Au/Gr/BPE are labeled in Fig. S29, with the fitted lattice constants and q_{hkl} values listed in Tables S3 and S4, respectively. Comparing with BPE powder, SiO₂/Gr/BPE and Au/Gr/BPE show expansion in b -axis and shrinking in c -axis, possibly due to the templating effect of graphene^{S35}. We find that the best-fitted lattice constants b and c for Au/Gr/BPE has about 1% expansion compared with that for SiO₂/Gr/BPE, corresponding to the increasing of interplanar distance between the PTCDI basal planes in Au/Gr/BPE.

Table S3. **Best fitted Lattice constants for BPE single crystal^{S39}, BPE powder sample, SiO₂/Gr/BPE and Au/Gr/BPE using monoclinic lattice model.**

	a (Å)	b (Å)	c (Å)	γ (°)
BPE single crystal ^{S39}	4.73	9.51	32.45	100.27
BPE powder	4.64±0.03	9.34±0.04	31.09±0.08	99.71±0.84
SiO ₂ /Gr/BPE	5.01±0.08	9.56±0.03	29.94±0.16	99.76±0.85
Au/Gr/BPE	4.87±0.09	9.67±0.04	30.29±0.27	100.28±1.03

S5.3 Breakdown of wetting transparency theory

An important evidence supporting the existence of repulsive vdW interaction in Au/Gr/BPE system is the breakdown of wetting transparency theory as observed from the lattice packing of BPE molecules on bare substrates. From the Lifshitz theory, the magnitude of attractive vdW interaction between substrate and BPE layer over vacuum monotonically increases when the dielectric responses of the substrate become stronger.

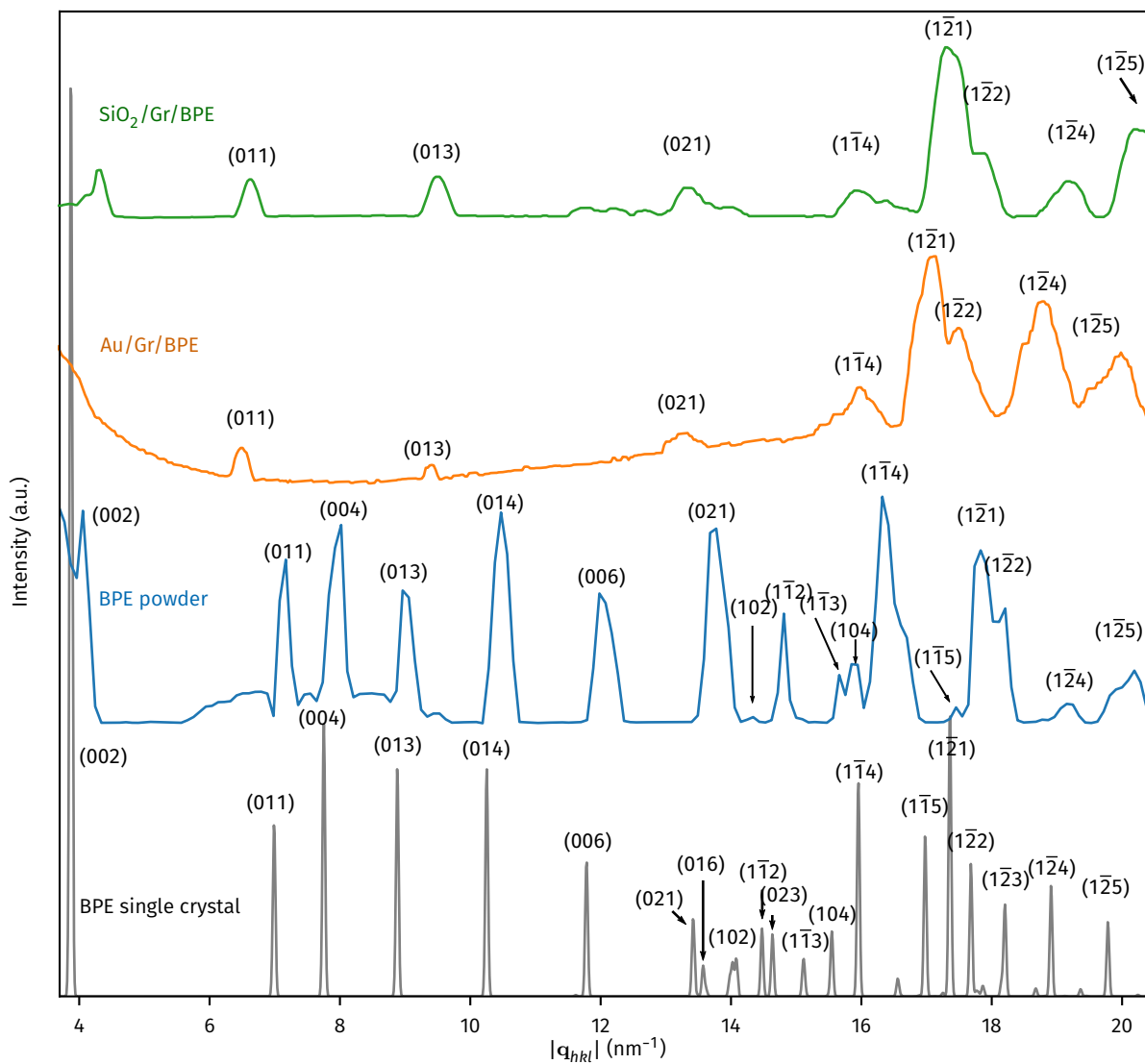


Fig. S29. 1D X-ray diffraction patterns of BPE single crystal, BPE powder, SiO₂/Gr/BPE and Au/Gr/BPE. The best-fitted (*hkl*) indices are labeled. Diffraction of BPE single crystal is simulated using the RIETAN-FP package within the VESTA software^{S41}.

Table S4. **Best fitted $|q_{hkl}|$ values of major Bragg diffraction peaks (hkl) for BPE single crystal^{S39}, BPE powder, SiO₂/Gr/BPE and Au/Gr/BPE using monoclinic lattice model.** Blank fields indicate the corresponding diffraction peaks are weak in the sample.

(hkl)	$ q_{hkl} $ (nm ⁻¹)			
	BPE single crystal ^{S39}	BPE powder	SiO ₂ /Gr/BPE	Au/Gr/BPE
(002)	3.87	4.04		
(011)	6.99	7.12	7.26	7.00
(004)	7.75	8.09		
(013)	8.88	9.13	9.38	9.13
(014)	10.25	10.58		
(006)	11.62	12.13		
(021)	13.57	13.80	13.61	13.37
(102)	14.03	14.32		
(1 $\bar{1}$ 2)	14.48	14.83		
(1 $\bar{1}$ 3)	15.11	15.51		
(104)	15.55	15.94		
(1 $\bar{1}$ 4)	15.95	16.40	16.02	15.99
(1 $\bar{1}$ 5)	16.98	17.49		
(1 $\bar{2}$ 1)	17.36	17.77	17.47	17.14
(1 $\bar{2}$ 2)	17.68	18.11	17.84	17.51
(1 $\bar{2}$ 4)	18.91	19.42	19.27	18.82
(1 $\bar{2}$ 5)	19.78	20.34	20.27	19.93

Therefore, when BPE molecules are evaporated on Au surface (Au/Vac/BPE), the vdW interaction potential becomes more negative compared with the SiO₂/Vac/BPE system, as shown in Fig. S30.

The change of substrate-BPE interaction leads to significant difference of BPE orientation between SiO₂/Vac/BPE and Au/Vac/BPE as measured from 2D GIWAXS spectra. The diffraction plane corresponding to the strongest Laue spot changes from (002) in SiO₂/Vac/BPE (Fig. S31a and S31c) to (013) in Au/Vac/BPE (Fig. S31b and S31d). The PTCDI planes are brought closer to the Au surface due to the stronger Au-BPE interaction compared with that on the SiO₂-BPE interface.

The classical wetting transparency theory for 2D materials^{S16,S17} clearly breaks down for the systems studied here. From the wetting transparency theory based on additive model of vdW interactions, stronger interactions between Au-BPE over vacuum will also lead to stronger vdW interactions in Au/Gr/BPE. Our observation of lattice expansion in Au/Gr/BPE clearly cannot be captured by classical wetting transparency theory.

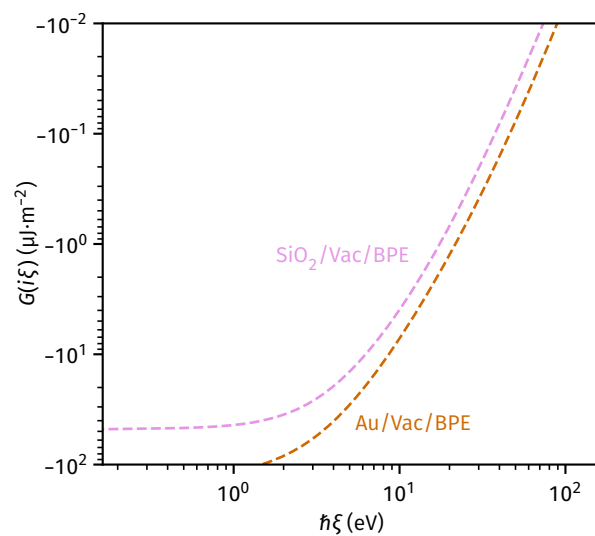


Fig. S30. **Single-frequency interaction energy $G(i\xi)$ as function for $\hbar\xi$ of BPE/Vac/SiO₂ (violet) and BPE/Vac/Au systems.** In contrast to the $G(i\xi)$ of graphene-mediated systems in Fig. 4b, the interaction between BPE and bare Au substrate is significantly stronger (more negative interaction potential) than that on bare SiO₂ substrate over the entire frequency range.

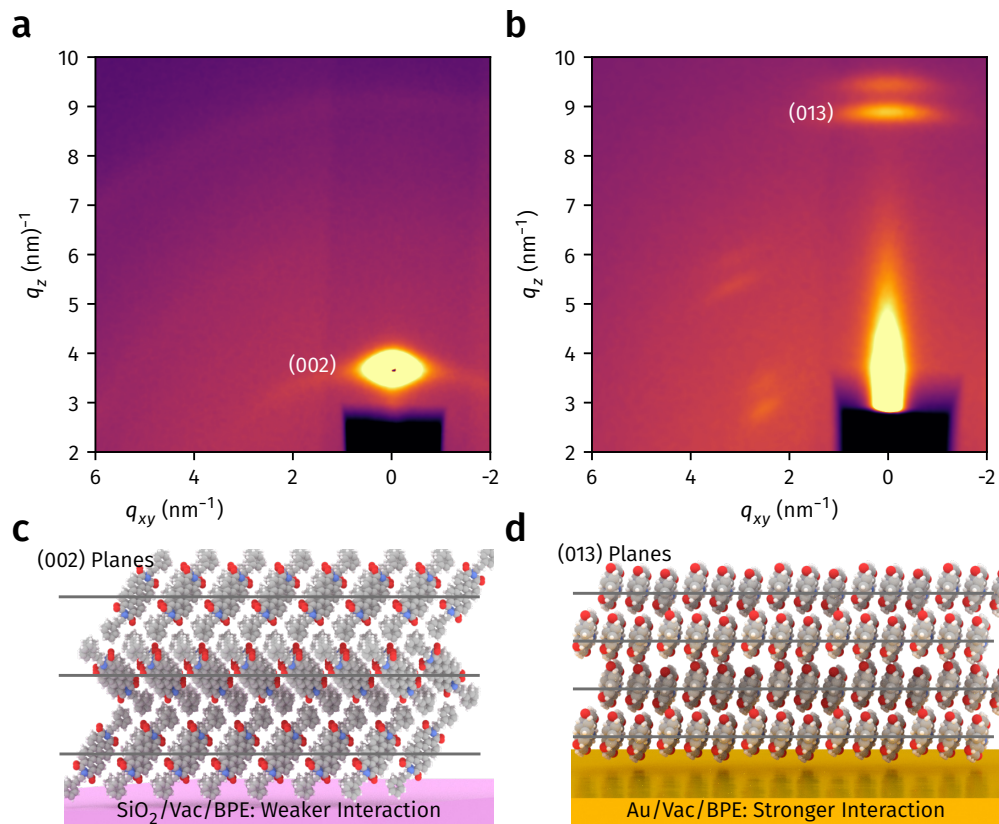


Fig. S31. GIWAXS spectra of BPE deposited on bare SiO₂ **a.** and Au **(b)** substrates. The principal peaks in BPE/Gr/SiO₂ and BPE/Gr/Au are (002) and (013) lattice planes, respectively. The larger distance of (002) compared with (013) lattice plane agrees with the stronger interaction in BPE/Vac/Au configuration. **c** and **d** Schemes of (002) and (013) lattice planes corresponding to **a** and **b**, respectively.

S6 Additional Discussions

This section contains further discussions that are not directly related to the results in the main text but may help understanding or extending our current work.

S6.1 Comparison with remote epitaxy and wetting transparency

In this section, we briefly compare our experimental observations with other known 2D material-induced phenomena, including the remote epitaxy^{S42-S44} (also known as the lattice transparency^{S45}) and wetting transparency^{S16,S17}. Both the remote epitaxy and wetting transparency are examples demonstrating the effect of substrate due to atomically-thin gap of 2D materials. Although the concept seems similar to our system, we argue that the underlying physics is substantially different.

Remote epitaxy

1. **Substrate polarity** The lattice transparency and remote epitaxy phenomena are dominated by the polarity of oriented dangling bonds at bulk material surface (such as GaAs or ZnO)^{S43}, while the phenomena observed in our experiments, the polarity of material deposited (either Au or BPE molecule) are much smaller. Increasing the polarity of substrate generally enhances crystalline quality of epitaxy layer under the lattice transparency picture. On the contrary, the polarity dependency fails to explain the crystal growth we observed on freestanding graphene, where the substrate essentially has no polarity.
2. **Length scale** Remote epitaxy or lattice transparency can only occur when the gap separating the substrate and the deposited material is very thin (typically a few Å)^{S42,S45}, in order to allow redistribution of electron density induced by the substrate. On the other hand, our theoretical analysis (Section S2) shows that the many-body vdW interaction can penetrate much longer distance, and is essentially controlled by dispersion interactions.
3. **Crystallinity of epitaxy layer** For Au deposition on various graphene surfaces, the crystalline quality is best on freestanding graphene surface (due to ultrafast diffusion), while in lattice transparency experiments, better crystalline samples are observed when the deposited material and the substrate are of the same lattice structure.

Wetting transparency

In principle, the wetting transparency theory is based on classical pair-wise vdW theory, which fails to capture any vdW repulsion. In both of our experimental demonstrations, the observations contradict the predictions based on wetting transparency:

Wetting on freestanding graphene From the classical wetting transparency theory, the total interaction energy Φ_{tot} between gold and the entire surface (S) (i.e. graphene + the underlying substrate) is expressed as: $\Phi_{\text{tot}} = \Phi_{S/\text{Au}} + \Phi_{G/\text{Au}}$, where $\Phi_{S/\text{Au}}$ is the total vdW interaction between the substrate and Au across vacuum, while $\Phi_{G/\text{Au}}$ is the manybody vdW interaction between monolayer graphene and Au over vacuum. Note here $\Phi_{S/\text{Au}}$ is hypothetical "two-body" interaction energies, i.e., independent of the existence of graphene between gold and the substrate. When S becomes vacuum, one can assume $\Phi_{S/\text{Au}} = 0$. From the classical wetting transparency model, $\Phi_{G/\text{Au}}$ is estimated to be $\sim 84\%$ of that between bulk graphite and Au^{S17}. In this sense, one would expect the adhesion of Au on freestanding graphene to be very close to that of Au on graphite. However, from our experimental results and KMC simulations, surface diffusion of Au on freestanding graphene is significantly faster than on graphite (Supplementary Fig. S25). In other words, making graphene freestanding contributes to additional reduction in the total vdW interaction, which we attributes to the many-body vdW repulsion in such configuration.

Molecular packing on substrate-supported graphene From the GIWAXS data of BPE molecules deposited onto bare SiO₂ and Au substrates (Section S5.3, Fig. S31), the PTCDI planes are brought closer to the substrate on Au/Vac/BPE configuration, indicating a stronger vdW interaction, which is also confirmed by our theoretical calculations (Fig. S30). If wetting transparency is the underlying phenomenon, one would expect to see that lattice packing in Au/Gr/BPE to be more closed-packed (if observable). However our GIWAXS analysis in main text Fig. 3 showed the opposite, indicating that an additional repulsive interaction exists in the system.

S6.2 Influence of bulk material bandgap

In principle, the vdW repulsion may also be observed on freestanding graphene even if the bulk material is semiconductor or insulator, as long as the inequality (1) in main text holds. Here we theoretically explore the influence of the bandgap of bulk material on the interfacial vdW forces in a Vac/Gr/B system, where B is

the bulk material with varied bandgap. Fig S32a compared the frequency-dependent dielectric functions for typical metal (Au), semiconductors (GaAs, GaN) and insulator (SiO_2) as compared with graphene at $d = 1$ nm. As a general trend, the dielectric response decreases for materials with larger bandgap. As a result, the

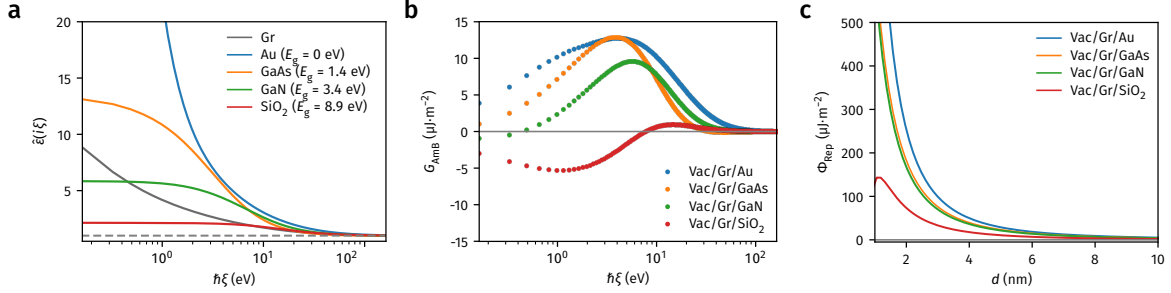


Fig. S32. **Influence of bulk material bandgap on the interfacial vdW repulsion** **a.** Dielectric functions for Au, GaAs, GaN and SiO_2 compared with graphene at $d = 1$ nm. **b.** Interaction spectra of Vac/Gr/B systems when B=Au, GaAs, GaN and SiO_2 , respectively. **c.** Distance-dependent vdW repulsion energy of corresponding system in **b**.

interaction spectra for Vac/Gr/B systems gradually shift to attractive at lower frequencies, when the bandgap of B increases (Fig. S32b and S32c). The results indicate that on freestanding graphene interface, it may be easiest to observe the vdW repulsion via epitaxy of metal, compared with semiconductors or insulators.

S6.3 Influence of 2D material layer number

An intuitive way to control the degree of interfacial forces on 2D materials is to control their layer numbers, which can also be captured by our theoretical framework. We model the many-body vdW interactions by extending the analysis in Section S2.2. For a system of Vac/NL-Gr/Au where NL-Gr represents N -layer graphene stacks, we assume that the polarizability of NL-Gr α_{NL}^p linearly scales with N^{S46} , such that

$$\alpha_{\text{NL}}^p = N\alpha_{2\text{D}}^p \quad (\text{S19})$$

where p is either in- or out-of-plane components and $\alpha_{2\text{D}}$ is the two-dimensional electronic polarizability of monolayer graphene.

Using this model, we calculated the distance-dependent total vdW interaction energy Φ_{tot} for the Vac/NL-Gr/Au system with varied layer numbers, as shown in Fig. S33. As expected, with increasing layer number of graphene, the contribution of repulsive interactions decreases and the repulsive barrier diminishes. We

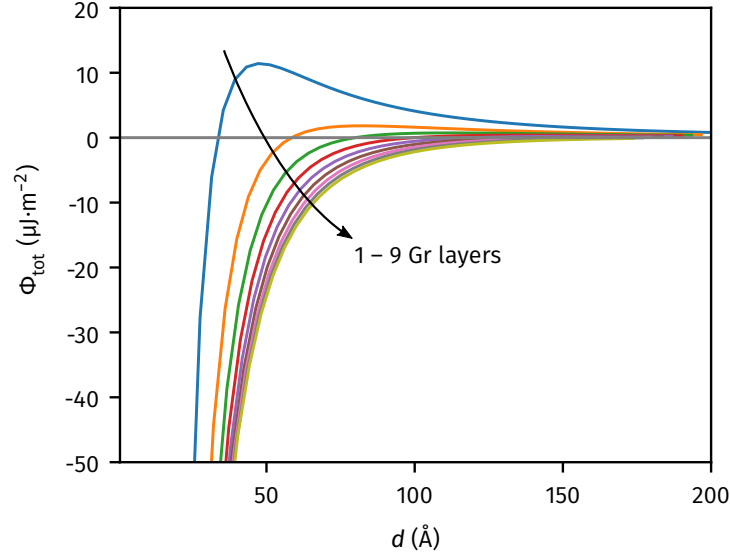


Fig. S33. **Total vdW interaction energy for Vac/NL-Gr/Au system with various graphene layer numbers.** With increasing graphene layer thickness, the repulsive barrier diminishes.

propose that such change of interaction can be probed by observing metal epitaxy on freestanding graphene with controlled numbers, which can be prepared using mechanical exfoliation techniques.

S6.4 Choice of 2D material

Another degree of freedom for controlling the interfacial forces is to change the kind of 2D material, in other words, replacing graphene with MoS₂ or hBN. Simple analysis of Eq. (S4) shows that $\Phi_{\text{AmB}}^{\text{vdW}}$ depends on:

1. **Dielectric mismatch:** $\Delta_{\text{Am}}\Delta_{\text{Bm}}$
2. **Dielectric anisotropy of m :** g_m

For isotropic medium m , $g_m = 1$. The maximal vdW repulsion at certain frequency ξ can be achieved when:

$$\frac{\partial \Delta_{\text{Am}}(\xi)\Delta_{\text{Bm}}(\xi)}{\partial \hat{\epsilon}_m(\xi)} = 0 \quad (\text{S20})$$

by definition of Δ_{Am} and Δ_{Bm} this is equivalent to $\hat{\epsilon}_m(\xi) = \sqrt{\epsilon_A(\xi)\epsilon_B(\xi)}$. However, using a 2D material as medium, we have $g_m < 1$, and g_m becomes smaller when the bandgap of 2D material decreases^{S46}. Therefore the situation is more complex than homogeneous medium. Our theoretical analysis in Fig. S34 shows that, when the effect of 2D anisotropy is considered, hBN actually have stronger repulsive interaction than graphene in the Vac/ m /Au systems, due to less screening at lower frequencies. The results indicate

that similar epitaxy morphology may also be observed on other freestanding 2D materials, which we will investigate in future studies.

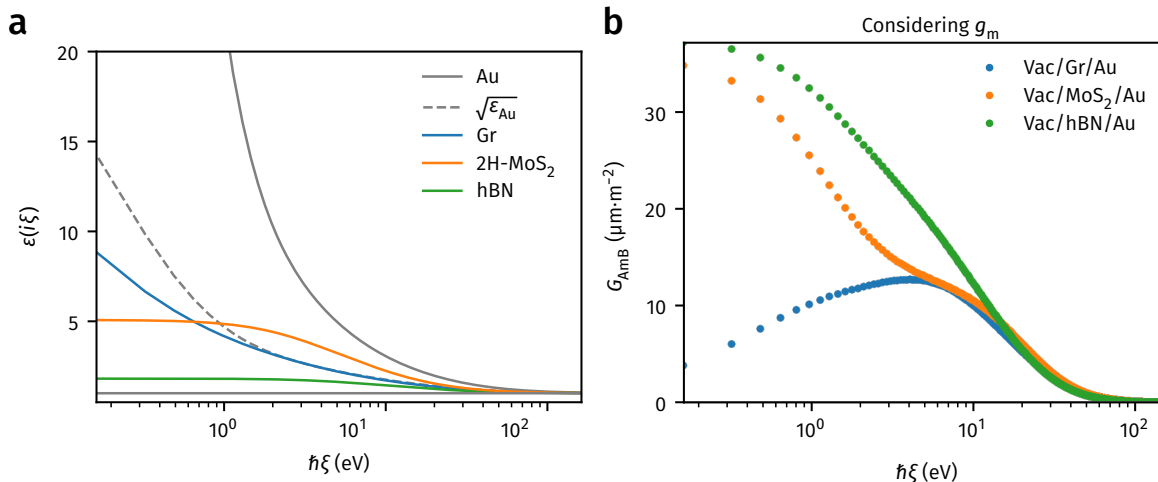


Fig. S34. **Influence of choice of 2D material.** **a.** Frequency-dependent dielectric responses for graphene, MoS₂, hBN at $d = 1$ nm. **c.** Interaction spectra in **b** when effect of g_m taken into account.

S6.5 Potential applications of repulsive 2D interface

The realization of repulsive vdW interactions at solid-state interface by the existence of 2D material layers opens up opportunities for practical applications, which we briefly discuss in the following topics:

Two-dimensional epitaxy Following our demonstration of ultrathin metallic platelets grown on free-standing graphene surface, the new 2D epitaxy mechanism can gain more practical impact if:

1. Precision control over nucleation site:

It is straightforward that if we can further control the location where the seed nuclei start to grow, such as via defect growth or ion beam drilling, it becomes possible to grow ultrathin and flat metallic thin films in a scalable manner.

2. Extending to larger variety of metals

In principle the method does not limit the choice of metal, because basically all metals have higher dielectric response than graphene. It is noteworthy that the growth of ultrathin and flat metallic thin films has been very challenging due to the high surface energy. The state-of-the-art organometallic

and colloidal chemistry only enables the synthesis of limited number of metallic platelet dispersions in solution, such as Au, Ag, and Al. The vdW-repulsion-induced 2D epitaxy of metal thin films is expected to be very impactful in the fields of plasmonics and optoelectronics.

3. Growing ultrathin semiconductor layers

In addition, following our earlier discussions, Fig. S32 implies that the scenario of 2D epitaxy may also apply to the growth of ultrathin semiconductors, which may be also of interests for next-generation electronics.

Molecular Sensors and Actuators The theoretical framework presented here allows us to predict the vdW interactions between a number of given molecules and different substrates through 2D monolayers. In principle, by coating a layer of rationally chosen 2D material onto a designed substrate, one can selectively make the vdW interactions being repulsive for a given molecule. Accordingly, this would become a new sensing mechanism to selectively adsorb analytes at a single-molecular level by designing a 2D material-coated substrate. An important advantage for this mechanism is that one can in principle design and screen all analytes and substrates *in silico*. Together with the freestanding 2D materials systems, another interesting sensing platform one can imagine is to first deposit ultrathin and flat 2D metal on one side of 2D monolayer, followed by sensing the adsorption events of molecular analytes on the other side by the near-field Raman spectroscopy (for example, in proximity to an AFM setup). The combination of surface-enhanced Raman spectroscopy and Lifshitz-vdW interactions may allow to detect molecular adsorption down to single molecular level.

References

- S1. Parsegian, V. A. *Van der Waals Forces: A Handbook for Biologists, Chemists, Engineers, and Physicists* Cambridge Core. (2017).
- S2. *Handbook of optical constants of solids* (ed Palik, E. D.) (Academic Press, 1998).
- S3. Munday, J. N., Capasso, F. & Parsegian, V. A. Measured long-range repulsive Casimir–Lifshitz forces. *Nature* **457**, 170–173 (2009).

- S4. Gioti, M. & Logothetidis, S. Dielectric function, electronic properties and optical constants of amorphous carbon and carbon nitride films. *Diam. Relat. Mater.* **12**, 957–962 (2003).
- S5. Mortensen, J. J., Hansen, L. B. & Jacobsen, K. W. Real-space grid implementation of the projector augmented wave method. *Phys. Rev. B* **71**, 035109 (2005).
- S6. Kresse, G. & Joubert, D. From ultrasoft pseudopotentials to the projector augmented-wave method. *Phys. Rev. B* **59**, 1758–1775 (1999).
- S7. Perdew, J. P., Burke, K. & Ernzerhof, M. Generalized Gradient Approximation Made Simple. *Phys. Rev. Lett.* **77**, 3865–3868 (1996).
- S8. Huang, Y. *et al.* Reliable Exfoliation of Large-Area High-Quality Flakes of Graphene and Other Two-Dimensional Materials. *ACS Nano* **9**. PMID: 26336975, 10612–10620 (2015).
- S9. Schneider, G. F., Calado, V. E., Zandbergen, H., Vandersypen, L. M. K. & Dekker, C. Wedging Transfer of Nanostructures. *Nano Lett.* **10**, 1912–1916 (2010).
- S10. Hegner, M., Wagner, P. & Semenza, G. Ultralarge atomically flat template-stripped Au surfaces for scanning probe microscopy. *Surf. Sci.* **291**, 39–46 (1993).
- S11. Clark, N., Oikonomou, A. & Vijayaraghavan, A. Ultrafast quantitative nanomechanical mapping of suspended graphene. *Phys. Status Solidi B* **250**, 2672–2677 (2013).
- S12. Li, J.-L. *et al.* Use of dielectric functions in the theory of dispersion forces. *Phys. Rev. B* **71**, 235412 (2005).
- S13. Meurk, A., Luckham, P. F. & Bergström, L. Direct Measurement of Repulsive and Attractive van der Waals Forces between Inorganic Materials. *Langmuir* **13**, 3896–3899 (1997).
- S14. Zhou, Y., Pellouchoud, L. A. & Reed, E. J. The potential for fast van der Waals computations for layered materials using a Lifshitz model. *2D Mater.* **4**, 025005 (2017).
- S15. Zhou, Y. & Reed, E. J. Microscopic Origins of the Variability of Water Contact Angle with Adsorbed Contaminants on Layered Materials. *J. Phys. Chem. C* **122**, 18520–18527 (2018).
- S16. Rafiee, J. *et al.* Wetting transparency of graphene. *Nat. Mater.* **11**, 217–222 (2012).
- S17. Shih, C.-J. *et al.* Breakdown in the Wetting Transparency of Graphene. *Phys. Rev. Lett.* **109**, 176101 (2012).

- S18. Weisenhorn, A. L., Maivald, P., Butt, H.-J. & Hansma, P. K. Measuring adhesion, attraction, and repulsion between surfaces in liquids with an atomic-force microscope. *Phys. Rev. B* **45**, 11226–11232 (1992).
- S19. Kassies, R., van der Werf, K. O., Bennink, M. L. & Otto, C. Removing interference and optical feedback artifacts in atomic force microscopy measurements by application of high frequency laser current modulation. *Review of Scientific Instruments* **75**, 689–693 (2004).
- S20. Lee, C., Wei, X., Kysar, J. W. & Hone, J. Measurement of the Elastic Properties and Intrinsic Strength of Monolayer Graphene. *Science* **321**, 385–388 (2008).
- S21. Celebi, K. *et al.* Ultimate Permeation Across Atomically Thin Porous Graphene. *Science* **344**, 289–292 (2014).
- S22. Liang, X. *et al.* Toward Clean and Crackless Transfer of Graphene. *ACS Nano* **5**, 9144–9153 (2011).
- S23. Lin, Y.-C. *et al.* Graphene Annealing: How Clean Can It Be? *Nano Lett.* **12**, 414–419 (2011).
- S24. Cihan, E., İpek, S., Durgun, E. & Baykara, M. Z. Structural lubricity under ambient conditions. *Nat. Commun.* **7**, 12055 (2016).
- S25. Cihan, E., Özoğul, A. & Baykara, M. Z. Structure and nanotribology of thermally deposited gold nanoparticles on graphite. *Appl. Surf. Sci.* **354**, 429–436 (2015).
- S26. Cross, C. E., Hemminger, J. C. & Penner, R. M. Physical Vapor Deposition of One-Dimensional Nanoparticle Arrays on Graphite: Seeding the Electrodeposition of Gold Nanowires. *Langmuir* **23**, 10372–10379 (2007).
- S27. Zan, R., Bangert, U., Ramasse, Q. & Novoselov, K. S. Evolution of Gold Nanostructures on Graphene. *Small* **7**, 2868–2872 (2011).
- S28. Özoğul, A., İpek, S., Durgun, E. & Baykara, M. Z. Structural superlubricity of platinum on graphite under ambient conditions: The effects of chemistry and geometry. *Appl. Phys. Lett.* **111**, 211602 (2017).
- S29. Temiryazev, A., Frolov, A. & Temiryazeva, M. Atomic-force microscopy study of self-assembled atmospheric contamination on graphene and graphite surfaces. *Carbon* **143**, 30–37 (2019).
- S30. Wayman, C. & Darby, T. Nucleation and growth of gold films on graphite. *J. Cryst. Growth* **28**, 53–67 (1975).

- S31. Darby, T. & Wayman, C. Nucleation and growth of gold films on graphite. *J. Cryst. Growth* **28**, 41–52 (1975).
- S32. Hsieh, S. *et al.* Imaging and Manipulation of Gold Nanorods with an Atomic Force Microscope. *J. Phys. Chem. B* **106**, 231–234 (2002).
- S33. Lewis, L. J., Jensen, P., Combe, N. & Barrat, J.-L. Diffusion of gold nanoclusters on graphite. *Phys. Rev. B* **61**, 16084–16090 (2000).
- S34. Bardotti, L. *et al.* Diffusion and aggregation of large antimony and gold clusters deposited on graphite. *Surf. Sci.* **367**, 276–292 (1996).
- S35. Tian, T. & Shih, C.-J. Molecular Epitaxy on Two-Dimensional Materials: The Interplay between Interactions. *Ind. Eng. Chem. Res.* **56**, 10552–10581 (2017).
- S36. Yan, Z. *et al.* Controlled Modulation of Electronic Properties of Graphene by Self-Assembled Monolayers on SiO₂ Substrates. *ACS Nano* **5**, 1535–1540 (2011).
- S37. Das, A. *et al.* Monitoring dopants by Raman scattering in an electrochemically top-gated graphene transistor. *Nat. Nanotechnol.* **3**, 210–215 (2008).
- S38. Schindelin, J. *et al.* Fiji: an open-source platform for biological-image analysis. *Nat. Methods* **9**, 676–682 (2012).
- S39. Mizuguchi, J. N,N'-Bis(2-phenethyl)perylene-3,4:9,10-bis(dicarboximide). *Acta Cryst. C* **54**, 1479–1481 (1998).
- S40. Andrews, K. W., Dyson, D. J. & Keown, S. R. *Interpretation of Electron Diffraction Patterns* (Springer, 1967).
- S41. Momma, K. & Izumi, F. VESTA: a three-dimensional visualization system for electronic and structural analysis. *J. Appl. Cryst.* **41**, 653–658 (2008).
- S42. Kim, Y. *et al.* Remote epitaxy through graphene enables two-dimensional material-based layer transfer. *Nature* **544**, 340–343 (2017).
- S43. Kong, W. *et al.* Polarity governs atomic interaction through two-dimensional materials. *Nat. Mater.* **17**, 999–1004 (2018).

- S44. Lu, Z. *et al.* Remote epitaxy of copper on sapphire through monolayer graphene buffer. *Nanotechnology* **29**, 445702 (2018).
- S45. Chae, S. *et al.* Lattice Transparency of Graphene. *Nano Lett.* **17**, 1711–1718 (2017).
- S46. Tian, T. *et al.* Electronic Polarizability as the Fundamental Variable in the Dielectric Properties of Two-Dimensional Materials. *Nano Lett.* **20**, 841–851 (2019).